Stanford Geothermal Program
Final Report
July 1996 - June 1999

Funded by the
U.S. Department of Energy
under grant number
DE-FG07-95ID13370

Stanford Geothermal Program
Department of Petroleum Engineering
Stanford University
Stanford, CA 94305-2220
USA

Table of Contents

1. STEAM-WATER RELATIVE PERMEABILITY

1.1 SUMMARY

Reliable measurement of steam-water relative permeability functions is of great importance for geothermal reservoir performance simulation. Despite their importance, these functions are poorly known due to the lack of fundamental understanding of steam-water flows, and the difficulty of making direct measurements. The Stanford Geothermal Program has used an X-ray CT (Computer Tomography) scanner to obtain accurate saturation profiles by direct measurement. During the last five years, we have carried out experiments with nitrogen-water flow and with steam-water flow, and examined the effects of heat transfer and phase change by comparing these sets of results.

In porous rocks, it was found that the steam-water relative permeabilities follow Corey type relationships similar to those in nitrogen-water flow, but that the irreducible gas phase saturation is smaller for steam than for nitrogen. The irreducible saturations represent substantial fractions of the recoverable energy in place yet are hard to determine in the field. Understanding the typical magnitude of irreducible saturations will lead to a much clearer forecast of geothermal field performance. In fracture flow, indirect measurements suggested that the relative permeabilities follow a linear (or "X-curve") behavior -- but there is still considerable uncertainty in the knowledge of this behavior.

1.2 INTRODUCTION

The flow of steam and water through the interstices of geothermal rocks is governed by complex physical phenomena involving mechanical interaction between the two fluids, water and steam, as well as by the thermodynamic effects of boiling heat transfer. This complex interaction is commonly described in terms of the steam-water relative permeabilities, defined as a modification of Darcy's Law for single-phase flow:

$$q = \frac{k}{\mu} A \left(\frac{\Delta p}{L}\right) \tag{1.1}$$

where q, k, μ, A, L, Δp are volumetric fluid flow rate, absolute permeability, fluid viscosity, cross-sectional area, length and pressure drop over the length L, respectively. When steam and water flow simultaneously, each phase is governed by an independent flow equation:

$$k_i = k\, k_{ri} = \frac{q_i\, \mu_i\, L}{A\, \Delta p_i} \quad ; \quad i = steam, water. \tag{1.2}$$

Here k_i is effective permeability to phase i, q_i is volumetric fluid flow rate of phase i, and μ_i is viscosity of phase i. The nondimensional form of effective permeability, called the relative permeability (k_r), is defined as the ratio of effective permeability to absolute permeability ($k_{ri}=k_i/k$). Relative permeabilities are generally expressed as a function of the wetting phase saturation (usually water in the case of steam-water flow).

Steam-water relative permeabilities have been shown to make a significant impact on the performance of geothermal reservoirs (Bodvarsson, O'Sullivan and Tsang, 1980), however in practice they are extremely difficult parameters to measure. For homogeneous porous media the commonly assumed relative permeabilities are the Corey expressions (Corey, 1954):

$$
\begin{aligned}
k_{rl} &= S^{*4} && (S^* < 1) \\
k_{rg} &= \left(1 - S^*\right)^2 (1 - S^{*2}) && (S^* < 1) \\
S^* &= \left(S - S_{lr}\right) / \left(S_{gr} - S_{lr}\right)
\end{aligned}
\tag{1.3}
$$

where S_{gr} and S_{lr} are the irreducible or residual saturations for liquid and gas, respectively. For fractured media, it has been more common to assume that the relative permeabilities follow the linear relationships known as the "X-curves":

$$
\begin{aligned}
k_{rl} &= S^* && (S^* < 1) \\
k_{rg} &= \left(1 - S^*\right) && (S^* < 1) \\
S^* &= \left(S - S_{lr}\right) / \left(S_{gr} - S_{lr}\right)
\end{aligned}
\tag{1.4}
$$

where it is common to assume the residual saturations S_{gr} and S_{lr} to be zero. These two types of relative permeability curve are illustrated in Figure 1.1.

The principal problems in obtaining steam-water relative permeabilities experimentally are in measuring: (1) the in-place saturations, and (2) the flow rates of the two phases. In oil-water relative permeability experiments, the saturations and flow rates are determined easily by direct measurement of the inflows and outflows of the two phases, but in the case of steam and water the phases can easily change from one to the other, hence the difficulty. Table 1.1 summarizes 25 years of work in the determination of steam-water relative permeability, including the methods used to measure saturation. Despite the number of independent studies, the results have proven to be inconsistent, hence confidence in the use of the results for commercial reservoir simulation has been low.

The Stanford Geothermal Program has conducted steam-water relative permeability experiments in two campaigns, one in the 1970s (Arihara, 1974, Chen et al., 1978, Counsil and Ramey, 1979) and more recently in the 1990s (Ambusso, 1996, Tovar, 1997, Satik, 1998, Mahiya, 1999). Since 1996, the Stanford measurements have used X-ray CT (Computer Tomography) methods to determine the in-place steam saturation. This powerful and accurate method allows for the steam-water distribution to be obtained at any place within the core (see Figure 1.2). Nonetheless, repeated studies still had difficulty in producing repeatable results that were consistent with earlier literature – the difficulty of determining the individual steam and water flow rates remained. One of our first successful measurements was by Ambusso (1996), Figure 1.3, who suggested that the steam-water relative permeabilities were best described by the X-curves. However, later measurements by Satik (1998), Figure 1.4, failed to confirm this, and indicated that Corey type behavior was more likely (as had also been seen elsewhere for unconsolidated materials by Sanchez and Schechter, 1990).

The study by Sanchez and Schechter (1990) had used an adiabatic experiment, maintaining the heat in the sample by use of guard heaters. The experiments of Ambusso (1996) and Satik (1998) were nonadiabatic, mainly because ferrous heaters placed around the core would attenuate the X-rays and cause artifacts in the saturation measurement. In the nonadiabatic experiments, the phase flow rates were computed after carefully measuring the heat fluxes from the core; nonetheless, this computation increased the uncertainty of the results. Since the results of Satik (1998) differed from those of Ambusso (1996) (although similar to the results of Sanchez and Schechter, 1990) and were difficult to reproduce, in 1999 Mahiya undertook a new study,

combining the adiabatic approach of Sanchez and Schechter (1990) with the X-ray CT measurement of saturation as used by Satik (1998). The study used a very thin film heater which avoided the problem of X-ray attenuation. The measurements attained by Mahiya (1999) demonstrated repeatability of Satik's 1998 results, and were close to those of Sanchez and Schechter (1990). Thus it was finally possible to associate confidence to these measurements, and to conclude that steam-water relative permeability relationships are of the Corey type. The measurements and experimental methodology described by Mahiya (1999) will be one of the main topics of this paper.

1.3 EXPERIMENTS

The physical parameters required to establish relative permeability curves are pressure, temperature, heat flux, flow rates and saturation. The experimental apparatus used by Satik (1998) and Mahiya (1999) made use of a nonmetallic coreholder made of the material PEEK, with a series of pressure and temperature measurements made along the interior axis of the core. Steam and water were injected independently into two separate ports at the inlet end of the coreholder, each with their own positive-displacement pump. The water used for injection was deaerated by preboiling, and then reheated by immersion heaters that were constructed within the inlet endplate of the coreholder. This configuration reduced heat losses between the heater and the core entry that had been a concern to Sanchez and Schechter (1990). Heat losses from the core were cancelled out using thin-film guard heaters under automatic computer control.

1.3.1 Experimental Configuration

Figure 1.5 shows a schematic of the apparatus that allowed real-time measurement of the required quantities. The experiment used a 43 cm Berea sandstone core with a nominal absolute permeability of 1200 md and a measured porosity of 24%. This was the same core used in experiments by Satik (1998). Pressures and temperatures were measured through ports at eight positions along the core spaced 5 cm apart. These ports connected the core to pressure transducers via plastic tubings, and provided tapping points into which thermocouple wires were inserted for temperature readings. A blanket of insulating fiber around this assembly partially reduced the escape of heat.

In order to achieve two-phase conditions in the core, dry steam and hot liquid water were injected separately into two ports at the inlet using two independent constant-displacement pumps. Injection rates were typically between 0 and 10 ml/min. Each stream of fluid used deionized water pumped from a common reservoir to a boiler and then to a condensing loop. This process eliminated dissolved air that would introduce errors in the saturation measurements. The deaerated water was then delivered to the heating head in the core inlet where each of the two streams was reheated to either steam or hot water. Steam and water then became mixed in the first few centimeters of the porous medium. Injection temperatures were typically of order 120ºC, although the value varied somewhat from one step to the next. Fluid exited the core at atmospheric pressure and was directed to the sink where volumetric rate was checked using a graduated cylinder and timer, and compared with the injection rates specified at the two inlet pumps.

In-situ saturation values were determined from CT image arrays generated by the X-ray CT scanner. The core assembly was mounted and secured on a stepper motor that allowed movement of the core in and out of the X-

ray gantry with 1 cm interval. We were able to take measurements at 41 sections along the core. Figure 1.6 shows the major components of the experimental apparatus and the CT scanner.

1.3.2 Flexible Guard Heaters

Despite the thick layer of insulation around the coreholder, there was still considerable heat escaping from the core in Satik's 1998 experiments. In the new experiment, the exact amount of heat that was lost was supplied back to the system, so that overall heat loss would be negligible, if not zero. We designed flexible heaters custom-made for this purpose. Figure 1.7 shows a schematic of one of the Kapton-insulated flexible heaters.

Since single-sheet heaters long enough to completely cover the core were not available, we used two separate 20×25 cm and 23×25 cm sheets. Holes with 1.34 cm diameters were provided to allow for the protruding pressure ports along the core length. Each sheet was an array of eight or nine 2.5×25 cm strips of heating elements that could be controlled independently. In effect, we had 17 different heaters, each rated at 0.4 W/cm^2 at 115 volts. Since the heaters required only a small amount of current to operate, we used a transformer to step-down the voltage from 120 VAC to 60 VAC. The flexible thin-film heaters did not cause significant X-ray interference.

Each of the 17 independent heating strips was controlled in response to its own heat flux sensor placed under the heater on the surface of the coreholder. The voltage to the heater strip was switched on and off with an on-time sufficient to supply enough heat to balance the energy being lost from the core. In most cases the switching cycle was 20-30 times a minute. Each strip was controlled independently, using a 32-channel National Instruments SCXI 1163-R solid-state relay output module.

1.3.3 Experimental Process

The core preparation procedure involved drying the core by subjecting it to 120ºC in an oven and simultaneously pulling a vacuum. The core had previously been baked at higher temperatures for the purpose of deactivating clays in the rock. Once dried, the core was assembled into the coreholder, and bonded in place using epoxy. A dry X-ray scan was then made to obtain the CT attenuation values CT_{dry}. The core was then fully saturated with water and scanned to obtain the values of CT_{wet}, and from these the porosity distribution was obtained. The next step was to flow hot liquid water to obtain CT_{hw} which was necessary for calculating experimental saturations. The completion of this scan marked the start of the actual flow-through experiments. The electrical power was increased in stages by changing the voltage settings of the two heaters that generated dry steam and hot water. During this staged procedure the wetting phase (water) was displaced by the nonwetting phase (steam) and hence the flow was a drainage process. At each stage, two-phase flow in the core was allowed to stabilize before an X-ray scan was performed. Pressure, temperature and heat fluxes from the core were measured at every stabilization. The maximum steam saturation was reached by injecting only steam at the inlet. Once maximum steam saturation was achieved, input power to the steam and water heaters was gradually decreased to create an imbibition process whereby liquid water displaced steam. The values of relative permeability to steam and water were then computed after choosing sections of the core in which the saturation could be seen (in the CT scans) to be constant. One important aspect of the computation was the requirement to correct for the Klinkenberg slip effect, as described by Li and Horne (1999).

1.3.4 Results

The results of the 1999 experiments by Mahiya are shown in Figure 1.8. The behavior of the relative permeability curves in these measurements is clearly of the Corey type, and shows little difference between drainage and imbibition processes. The relative permeability values are in close agreement with the values of both Satik (1998), for the same rock, and with the values of Sanchez and Schechter (1990), for an unconsolidated sand. Figure 1.9 shows the comparison in terms of k_{rs} vs. k_{rw}, showing the agreement between these three measurements, and the substantial difference of the results of Ambusso (1996). Also shown on Figure 1.9 are the relative permeability values for nitrogen and water (imbibition process), as measured by Li and Nassori in the same core and experimental apparatus used by Mahiya (1999) – although similar in shape, it is clear that the relative permeability to nitrogen is less than that to steam, mainly because the irreducible nitrogen saturation (about 0.3) is significantly greater than the irreducible steam saturation (about 0.2). The same data, plotted as a function of water saturation in Figure 1.10 shows that it is the gas relative permeability that differs most prominently betweem steam and nitrogen -- the water relative permeabilities are almost the same.

Although we may call the results of the experiments of "Corey type", in fact the values of the relative permeabilities are better fit to more general relations, of the type suggested by Honarpour et al. (1982):

$$k_{rs} = k_{rs0}\frac{(1-S_w-S_{sr})^{n_s}}{(1-S_{wr}-S_{sr})}$$
$$k_{rw} = k_{rw0}\frac{(S_w-S_{wr})^{n_w}}{(1-S_{wr}-S_{sr})} \qquad (1.5)$$

where S_{wr} and S_{sr} are the water and steam irreducible saturations respectively. Figure 1.11 shows a match to the data from the combined drainage and imbibition results of Mahiya (1999). The values of the best fit parameters are k_{rs0} = 0.63, k_{rw0} = 0.49, S_{sr} = 0.13, S_{wr} = 0.27, n_s = 2.04 and n_w = 2.65. The value of n_s (2.04) is very close to the Corey value of 2 from Eq. (1.3), while the value of n_w (2.65) is less than the Corey value of 4.

1.4 FRACTURE FLOW EXPERIMENTS

The relative permeabilities resulting from multiphase flow in fractures have received considerably less attention in published literature than those in porous media. The classically assumed X-curves (Figure 1.1) originated from experiments by Romm (1966) using oil-water flow in smooth fractures divided into strips in the flow direction. In Romm's experiments, the limiting values of the relative permeabilities k_{ro0} and k_{rw0} were both 1.0, and the residual saturations were both 0.0. That is, the sum of the relative permeabilities would always be one. More recent oil-water experiments in smooth fractures by Pan et al. (1996) also showed the residual saturations to be both 0.0, but the limiting k_{ro0} and k_{rw0} values were less than 1.0. Similar results were inferred in air-water flow in rough-walled fractures by Rangel-German et al. (1999).

Other experiments in rough-walled fractures have shown different kinds of relative permeability behavior. Fourar et al. (1993) conducted air-water experiments in both smooth- and rough-walled fractures, and proposed that the relative permeability concept was not useful to describe multiphase flow in fractures since the apparent relative permeability values would be functions of velocity. Even so, the apparent relative permeability curves shown in Fourar et al. (1993) do not appear to follow either X-curve or Corey behavior at any velocity. Persoff and Pruess (1995) measured air-water relative permeabilities in rough-walled fractures, and also

concluded that the values differ from either Corey or linear behavior (showing lower values than either of those two models, see Figure 1.12).

The theoretical study by Pruess and Tsang (1990) suggested that relative permeabilities in fractures may add up to considerably less than one, although the theory specifically excludes the possibility of "blobs" of one phase being conveyed by the other. The study also predicted ranges of saturation values at which neither phase can flow at all. In another study that released the "blob transport" exclusion, Rossen and Kumar (1992) advanced a theory that suggests a range of possibilities between the "sub-Corey" results of Pruess and Tsang (1990) at the lower end and the X-curves at the upper end.

All of the experimental studies mentioned so far in this section have been for air-water or oil-water flow. However, in fractures steam-water flow experiments have proven to be much more difficult, for the same reasons described in Section 1 for porous media. In one study, Wang and Horne (1999) inferred the steam-water relative permeabilities indirectly from experiments in a rough-walled fracture made of two plates of shower glass. 100°C water and steam flowed radially inward through the fracture towards a central port at which a vacuum was applied. Matching the observed temperature distribution in the fracture revealed that the observations could be replicated using a numerical simulation only if the relative permeability model was of the X-curve type (Figure 1.13).

1.5 DISCUSSION

The combined results of Satik (1998) and Mahiya (1999) established repeatability of the relative permeability measurements, and confirmed that these parameters follow the Corey type of behavior for flow in a porous rock. The similarity to the measurements of Sanchez and Schechter (1990) in unconsolidated sand adds further credence to this observation.

An important question to be raised is why the results of Ambusso (1996) were so different. The prominent deviation found by Satik (1998) provided significant confusion as to which of the two styles of relative permeability curve is the more appropriate. The confirming measurements by Mahiya (1999) suggest that it is the Corey type of behavior that is correct. It could be concluded that the rock in the Ambusso (1996) experiment had cracked, perhaps at the epoxy confinement, or maybe that the less sophisticated method of determining steam and water flow rates resulted in greater experimental error.

1.6 CONCLUSIONS

1. Steam-water relative permeabilities in a porous rock have been shown to follow Corey-type behavior.
2. This behavior has been confirmed in repeated experiments, and by comparison with earlier published results.
3. Proper interpretation of steam-water experiments at close to atmospheric pressure must include the influence of Klinkenberg slip effect.
4. Steam-water flow is similar to nitrogen water flow, except that the relative permeability to steam is greater than that to nitrogen, and the irreducible nitrogen saturation is greater than the irreducible steam saturation.

5. Steam-water relative permeabilities for flow in fractures are still unknown. Some steam-water and oil-water fracture flow experiments imply X-curve (linear) type of behavior, however other experiments using air and water imply even lower phase mobility than would be implied by Corey-type behavior.

In a real geothermal rock, steam and water will flow simultaneously in both fractures and in the porous matrix. The combination of these two flow processes may result in an effective relative permeability behavior that differs from either the Corey-type or the X-curve type of flow. The effect of this combination of behaviors has yet to be determined.

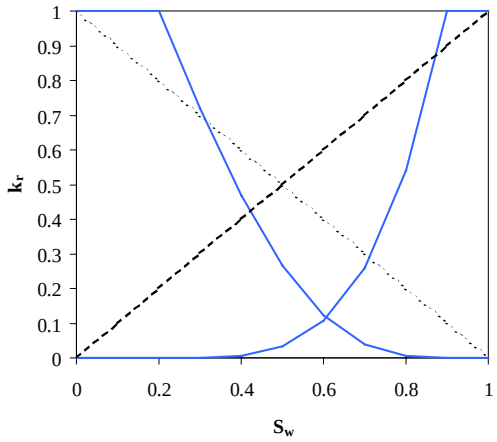

Figure 1.1: Corey (solid lines) and linear (dashed lines) relative permeability curves.

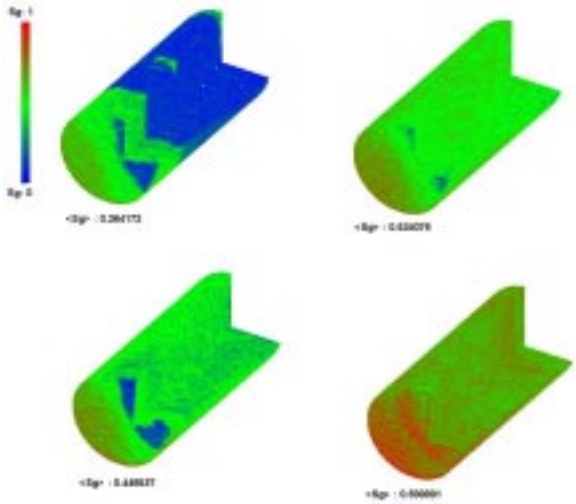

Figure 1.2: Steam distributions measured by X-ray CT, from Satik (1998).

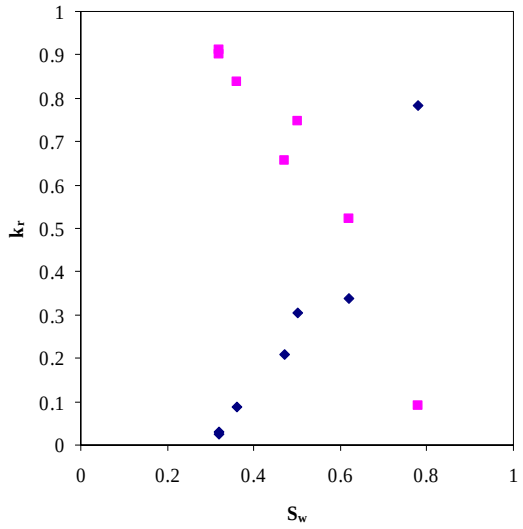

Figure 1.3: Experimental results from Ambusso (1996).

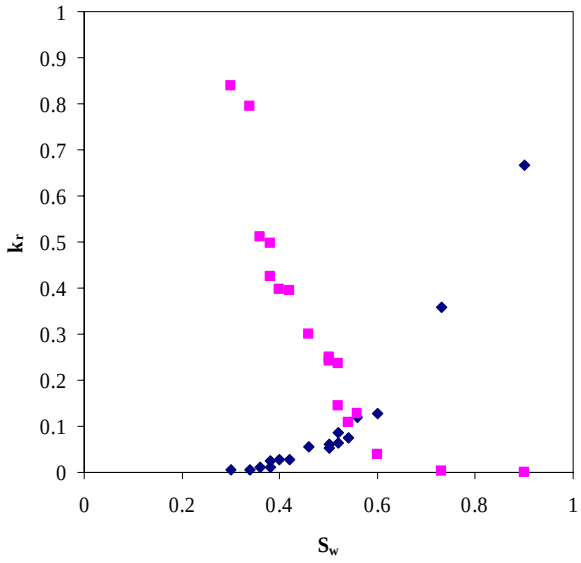

Figure 1.4: Experimental results from Satik (1998).

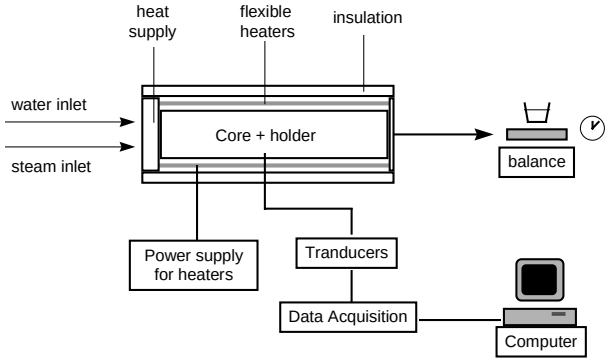

Figure 1.5: Experimental apparatus for the flow-through experiment using heat guards.

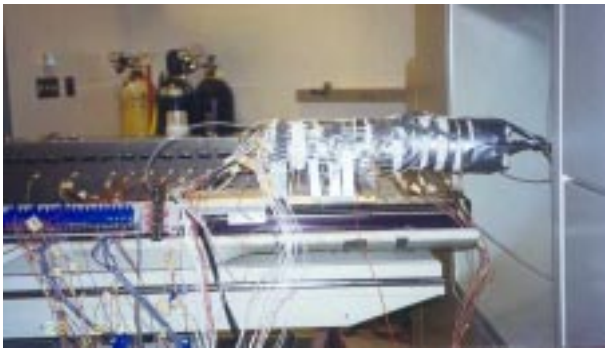

Figure 1.6: Core assembly mounted on stepper motor drive in the X-ray CT scanner.

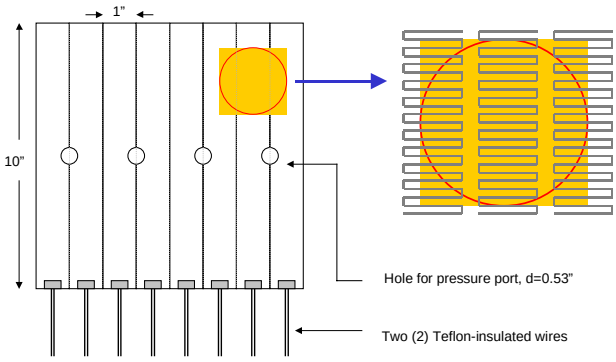

Figure 1.7: Schematic of flexible heaters.

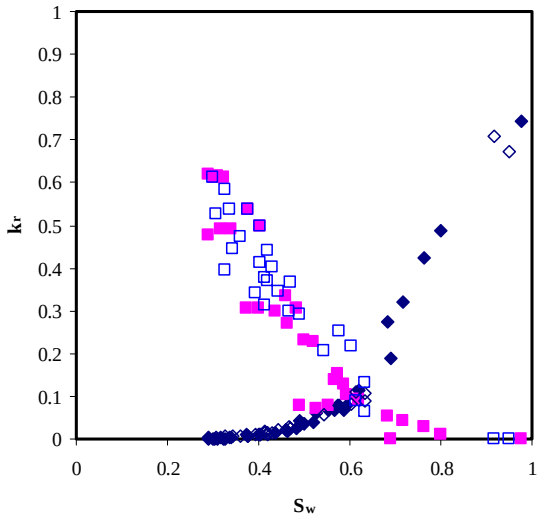

Figure 1.8: Experimental results from Mahiya (1999) adiabatic experiment. Closed symbols, drainage curves; open symbols, imbibition curves.

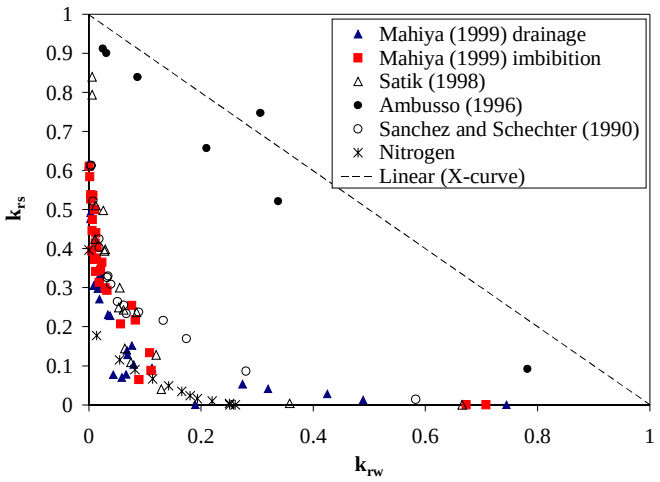

Figure 1.9: Comparison of results, k_{rs} vs. k_{rw}.

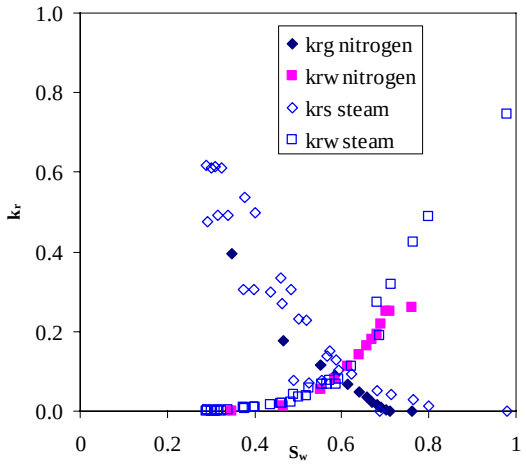

Figure 1.10: Comparison between steam-water (open symbols) and nitrogen-water imbibition (closed symbols) relative permeabilities on the same rock core.

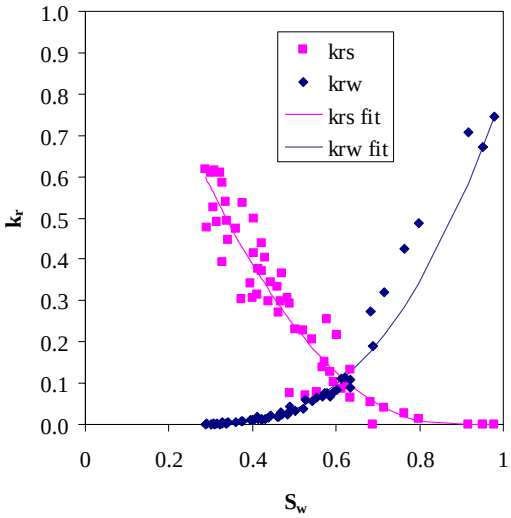

Figure 1.11: Fit to Mahiya (1999) results.

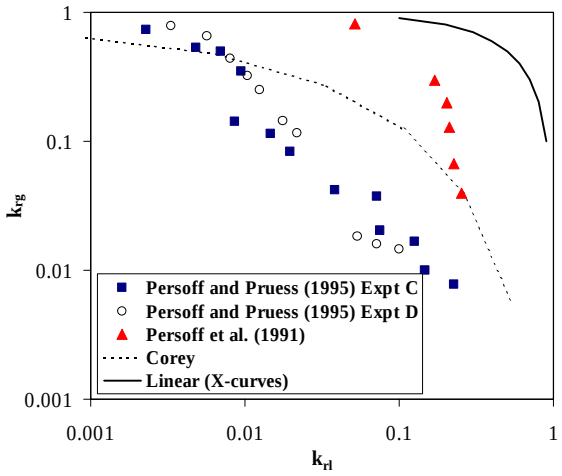

Figure 1.12: Some measurements of air-water relative permeabilities in rough-walled fractures.

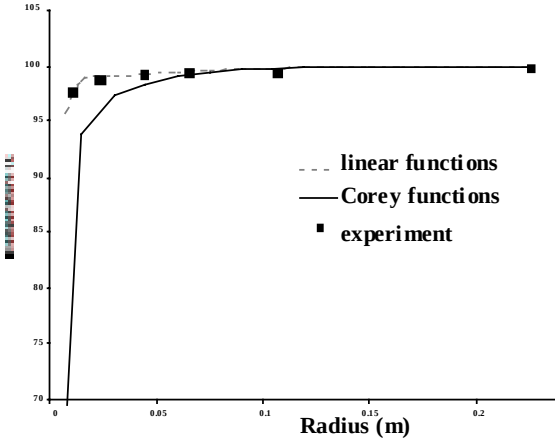

Figure 1.13: Fracture flow (temperature vs. radius) results from Wang and Horne (1999). Match using X-curves shown as dashed line, match using Corey curves shown as solid line.

Table 1.1: Previous experiments relevant to steam-water relative permeabilities, 1974-1999.

Reference	Year	Experiment type	Saturation technique	Core type
Mahiya	1999	Steam-water	CT scanner	Berea sandstone
Satik	1998	Steam-water	CT scanner	Berea sandstone
Ambusso	1996	Steam-water	CT scanner	Berea sandstone
Piquemal	1994	Steam-water	Gamma ray	Unconsolidated sand
Closmann and Vinegar	1988	Steam-water-oil	CT scanner	Natural core
Sanchez and Schechter	1987	Steam-water	Tracer	Unconsolidated sand
Verma and Pruess	1986	Steam-water	Gamma ray	Unconsolidated sand
Monsalve et al.	1984	Surfactant-steam-water	Tracer	Berea sandstone
Counsil and Ramey	1979	Steam-water	Capacitance probe	Consolidated synthetic
Horne and Ramey	1978	Steam-water	Production history	Field study
Chen et al.	1978	Steam-water	Capacitance probe	Consolidated synthetic
Grant	1977	Steam-water	Production history	Field study
Trimble and Menzie	1975	Steam-water-oil	Did not measure	Berea sandstone
Arihara	1974	Steam-water	Did not measure	Consolidated core

2. THE ROLE OF CAPILLARY FORCES IN THE NATURAL STATE OF FRACTURED GEOTHERMAL RESERVOIRS

2.1 INTRODUCTION

Much of the experimental work which pertains to geothermal systems has involved studies on porous media. Although most geothermal reservoirs are observed to be fracture dominated, experimental results involving porous media are often still applied. It is unclear whether a porous medium model is adequate in describing a fractured geothermal reservoir since there are some situations where the fractured nature of the reservoir cannot be ignored. One case involves the injection of cold brine (normally around 160°C) as a means of pressure support or for environmental reasons. If the geothermal system were to behave like a homogeneous porous medium, the thermal front would advance uniformly with the cooler fluid sweeping away the heat from the rock. In reality, this will not be the case. There will be a preferential flow through the fractures and even though there is transfer of heat by conduction from the rock to the cold water passing through the fractures, the injected water will arrive much sooner than in the case of a porous medium. Because of this problem, a dual porosity model is often invoked. Instead of treating the reservoir as homogeneous, fractures are introduced by dividing the system into two types of interacting porous media as can be seen in Fig. 2.1. The matrix is assigned a permeability, k_m, and a porosity, ϕ_m, while the fracture is assigned a higher permeability, k_f, and a higher porosity, ϕ_f.

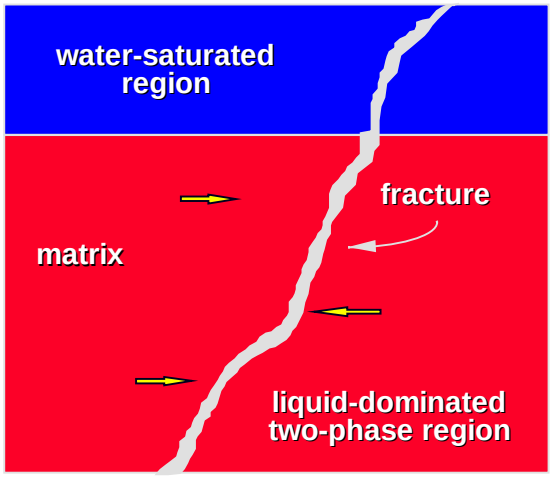

Fig. 2.1: A dual porosity model.

In a dual porosity model, the question of how heat is being transferred from the rock matrix to the fluid flowing in the fractures has been investigated. Previous works include those by Bodvarsson (1969, 1972), Drummond and McNabb (1972) and Nathenson (1975). The objective of this work was to further our understanding by investigating how heat and mass transfer is affected by capillary forces. To address this issue, it is worthwhile to investigate the heat pipe effect. The heat pipe mechanism (Eastman, 1968) allows the upward movement of heat in a system that exhibits a very small temperature gradient. Since this problem is reasonably understood from earlier work, looking into the heat pipe mechanism would enable us to understand the effect of capillary pressure on the behavior of fractured reservoirs.

White et al. (1971) proposed a conceptual model of a vapor-dominated geothermal reservoir. The model has a deep-seated convecting brine which is heated by a magmatic heat source. On top of this convecting brine is a two-phase region whose vapor and liquid phases undergo counterflow convection. This two-phase region is separated from the overlying zone of meteoric water and steam condensate by a caprock. For liquid-dominated systems, most of the conceptual models likewise invoke the presence of a caprock. Such is the case for the Tongonan geothermal reservoir in the Philippines (Grant and Studt, 1981) and the Wairakei geothermal field in New Zealand (Grindley, 1965).

Sondergeld and Turcotte (1977) did experimental studies on two-phase thermal convection in a porous medium. They were able to observe that a counterflowing two-phase zone can be stable beneath a water-saturated zone (Fig. 2.1). This experimental result suggests that geothermal reservoirs need not have to have a caprock. How is this possible? Will the presence of fractures destabilize the arrangements of fluids? What will be the influence of capillarity in permitting this configuration? One of the objectives of this study was to explore the stability of a water-saturated zone overlying a two-phase zone. The investigation on the stability of such systems was limited, however, to the case of a liquid-dominated two-phase reservoir.

To answer these questions, a numerical investigation was conducted utilizing the commercial program TETRAD (version 12). The approach utilized in this study involved the concept of building complexity. To start with, a one-dimensional numerical model was built in order to examine the heat pipe effect. This model was then extended to two dimensions. With this model the effect of capillary forces on heat and mass transfer as well as on stability was investigated by varying the capillary pressure curves.

2.2 PRELIMINARY WORK

Prior to the development of the two-dimensional numerical model used in this study, a one-dimensional numerical model was constructed in order to duplicate some of the results obtained by previous investigators who worked on heat pipes. Having a one-dimensional numerical model that conforms with experimental and theoretical results reinforces the validity of the model. Being confident with the one-dimensional model, the two-dimensional model was constructed in a similar fashion to the one-dimensional case. Since the numerical model now had two dimensions, the question of which differencing scheme, whether a five-point differencing scheme or a nine-point differencing scheme, is appropriate for the numerical model was raised. Likewise, the type of capillary pressure functions to be used in the study had to be determined.

2.2.1 One-dimensional model

The one-dimensional model consisted of a 7 m x 50 m x 1 m block and ten 7 m x 50 m x 50 m blocks stacked on top of each other as shown in Fig. 2.2. The model represents a homogeneous system and the properties assigned to each block are summarized in Table 2.1. The topmost block was given a very large volume in order to impose a constant pressure and saturation condition at the top. The blocks were initially saturated with water. With a 1 W/m^2 heat flux imposed at the bottom block, numerical simulation was carried out until steady state conditions were attained.

Table 2.1: Parameters of the one-dimensional model.

Property	Block 1 (Large volume element)	Blocks 2 - 11 (Matrix blocks)
Porosity	0.8	0.1
Permeability (md)	2000	0.5
Rock density (kg/m^3)	2643	2643
Rock conductivity (W/m-°C)	2.88	2.88
Rock specific heat (kJ/kg-°C)	1.0718	1.0718
Heat flux (W/m^2) - block 11		1.0
Relative permeability	$k_{rl} = (S)^3$ $k_{rv} = (1\text{-}S)^3$	$k_{rl} = (S)^3$ $k_{rv} = (1\text{-}S)^3$

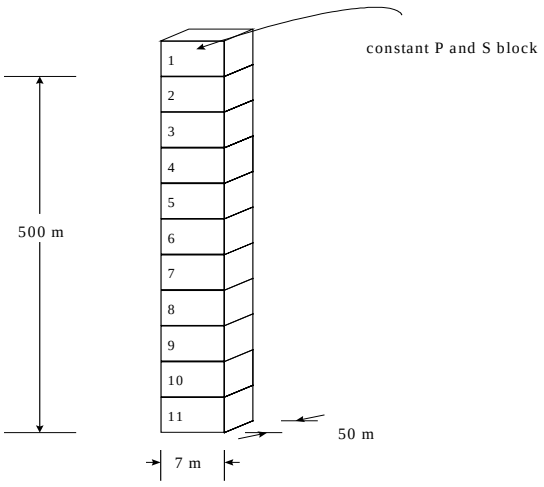

Fig. 2.2: One-dimensional model of a heat pipe.

Results indicated that two-phase conditions were present at a depth of 175 m (block no. 5) down to the bottom. In this two-phase region vapor rises up to block no. 5 while liquid trickles from block no. 5 down to the bottom. There was a counterflow of the liquid and the vapor phases within the two-phase zone. A plot of the dimensionless heat flux versus saturation is shown in Fig. 2.3. The analytical solution and the dimensionless heat flux for each block was derived for the cubic relative permeability curves (Table 2.1) utilizing the same procedure Bau and Torrance (1982) used. The dimensionless heat fluxes for each block were calculated using the following equation:

$$\Gamma = \frac{q\nu_v}{\lambda h_{lv} g(\rho_l - \rho_v)} = \frac{S^3(1-S)^3}{(1-S)^3 \frac{\nu_l}{\nu_v} + S^3} \tag{2.1}$$

where

Γ = dimensionless heat flux

q = vertical heat flux

ν_v = vapor kinematic viscosity

ν_l = liquid kinematic viscosity

h_{lv} = latent heat of vaporization

λ = permeability

ρ_l = liquid density

ρ_v = vapor density

g = acceleration due to gravity

S = liquid saturation

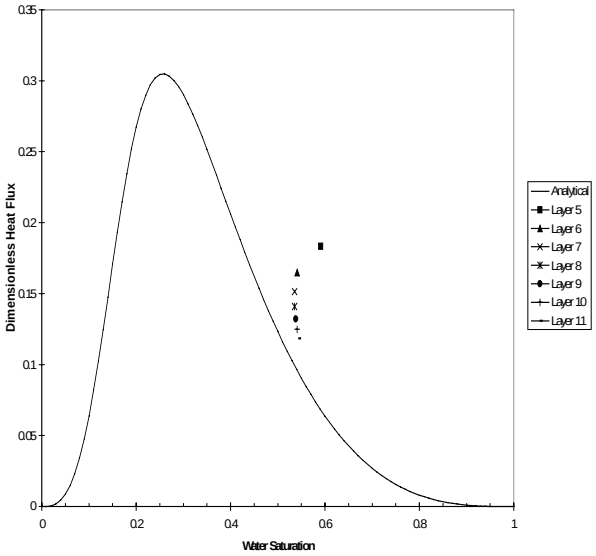

Figure 2.3: Plot of the dimensionless heat flux versus saturation for a cubic relative permeability curve.

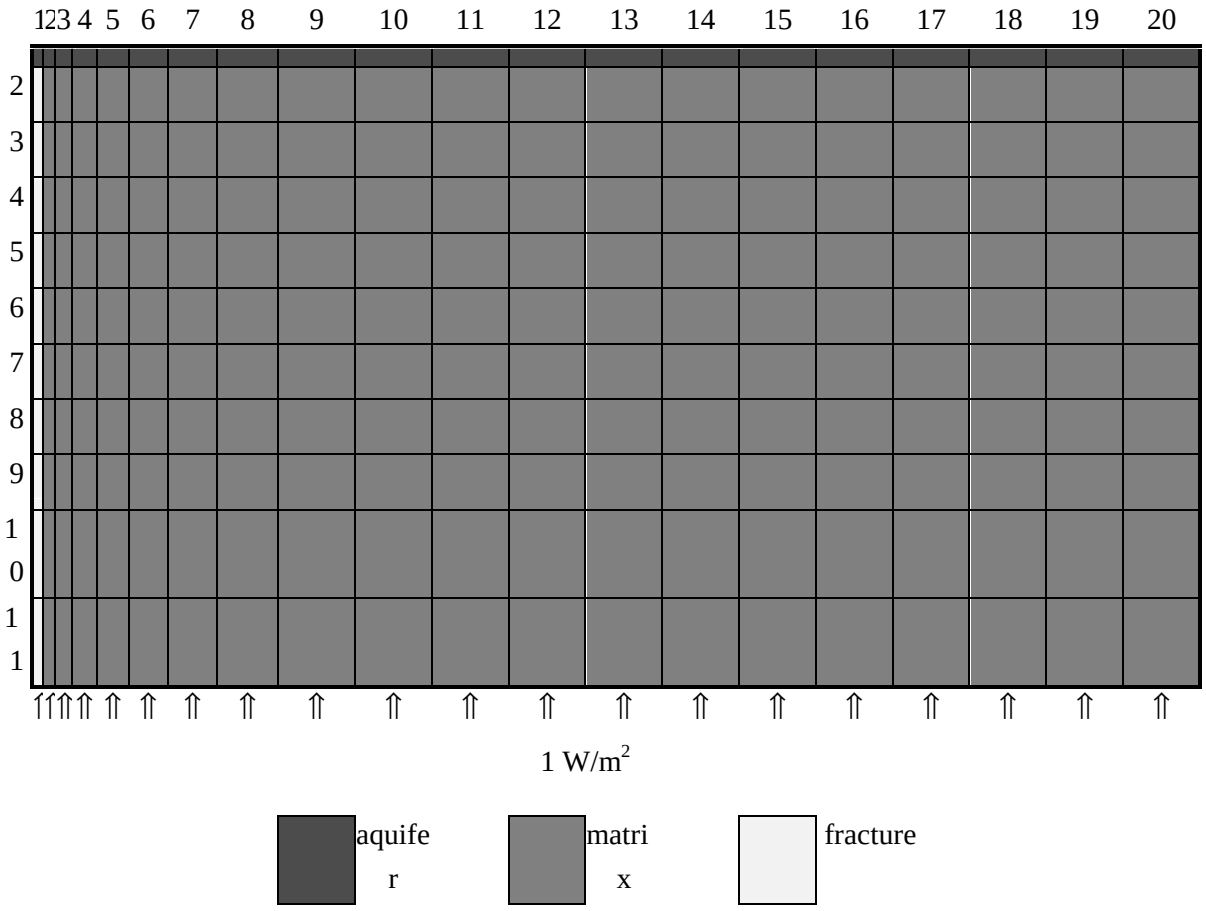

Fig. 2.4: The 20 x 11 x 1 block model.

The points do not plot on the line representing the analytical solution but instead lie to the right of it. One possible explanation is that the heat transfer mechanism in this one-dimensional system involves both convection and conduction, whereas the analytical solution does not take conduction into account. The graph however shows that we were able to produce a liquid-dominated heat pipe since the water saturations were above the saturation corresponding to the maximum heat flux, in this case, 0.26.

2.2.2 Two-dimensional model

With the existing one-dimensional model, a two-dimensional grid was produced by having 20 grid blocks in the x direction instead of just having one and maintaining the number of layers in the z direction. The grid system is shown in Fig. 2.4. The model had dimensions of 7 m x 501 m x 50 m and consisted of 220 blocks. The first two columns had a length of 0.01 m, the third column had a length that is twice that of the previous one and this progression continued until the seventh column had a length of 0.32 m. The eighth column had a length of 0.36 and the remaining 12 columns had a length of 0.5 m. The depth and width of each grid block was 50 m. The blocks in the first layer were assigned very large volumes and were fully saturated with water hence these large volume blocks were termed the aquifer

blocks. The rest of the blocks were labeled as matrix blocks. The same properties outlined in Table 2.1 were assigned to this two-dimensional numerical model. The same heat flux of 1 W/m^2 was delivered to the blocks at the bottom layer.

To achieve steady state, the model was ran up to a time of 4×10^6 days. The results showed no variation in the temperature, pressure and saturation values along the x direction in all the layers. Even though a two-dimensional grid was used, the system behaved like the one-dimensional case due to the fact that the system was homogeneous. Likewise, the graph of the non-dimensional heat flux as a function of water saturation looks exactly like Fig. 2.3. With this two-dimensional model, the stability of a water-dominated region over a liquid-dominated two-phase system was demonstrated.

The fact that the two-dimensional model with uniform matrix properties was able to duplicate the behavior of the one-dimensional model reinforces the validity of both models as well as that of the simulator itself. After having shown that a water-dominated region can be stable over a liquid-dominated two phase region, the next question was, how would this stability be affected by the presence of fractures.

The reason why the grid was designed as in Fig. 2.4 was in order to model a fracture on the left-hand side. Hornbrook and Faulder (1993) modeled a fracture by having large blocks (10 m wide) which were assigned a porosity of 0.0001 in order to simulate a 1 mm fracture. The fracture in this case was modeled by having blocks which were thin (0.01 m wide) and which were given a porosity of 0.5 in order to simulate a 0.005 m fracture. By specifying a larger permeability and porosity to the blocks in column 1 as compared to the matrix blocks (Fig. 2.4), a fracture at the left-hand side of the model was created. This two-dimensional model with both fracture and matrix blocks was the one used in the investigation.

2.2.3 Five-point versus nine-point differencing schemes

The standard approach in numerical simulation work is to make use of the five-point differencing scheme in the discretization of the differential equations describing reservoir flow. In a two-dimensional grid, the flow in and out of a computational grid point is influenced by the points directly to the sides, above and below it. With a higher order differencing scheme, such as a nine-point, the four computational grid points along the diagonals are also taken into account. Pruess (1991) indicated that although there are cases where the five-point differencing scheme is appropriate, there are certain situations where the nine-point differencing scheme is better. Pruess showed that a higher-order differencing scheme substantially diminishes the grid orientation effects. The study done by Hornbrook and Faulder (1993) asserted that the nine-point differencing scheme was more appropriate. The question then was, which differencing scheme is appropriate for the two-dimensional system in this study?

To address this issue, we made use of a 5 x 1 x 11 block numerical model whose properties were similar to the model described in Section 2.3.2. The dimensions, however, were 25 m x 50 m x 501 m. Using the five-point differencing scheme, the steady state solution was simulated. Three other simulation runs utilizing the five-point differencing scheme were performed using different models. The second

model had 10 blocks in the x direction while the third and fourth ones had 14 and 18 blocks, respectively. The numerical runs indicated that with the five-point differencing scheme, the results obtained were consistent. The steady state solution was independent of the grid system used.

A second set of simulation runs was conducted using the same set of models. However, this time the nine-point differencing scheme was utilized. Results indicated that the steady state solution for each run was dependent on the grid system used.

A comparison between experimental and numerical results was done in order to further examine the applicability of the five-point differencing scheme. The experimental results obtained by Bau and Torrance (1982) for a porous bed with permeability of 8.5 d were simulated using a radial grid model. The centerline temperatures obtained from experiments were compared to those obtained from the numerical model where a five-point differencing scheme was used. Fig. 2.5 shows that the numerical results replicate the experimental results especially in the two-phase regions.

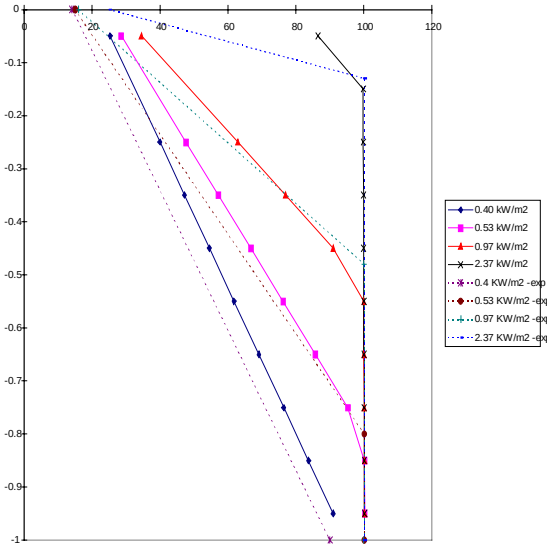

Fig. 2.5: A comparison between the centerline temperatures obtained from Bau and Torrance's (1982) experiment and the radial grid numerical model.

From these observations, we determined that the five-point differencing scheme was more appropriate than the nine-point differencing scheme for this type of problem. Hence, all the subsequent numerical runs used the five-point differencing scheme.

2.2.4 Capillary pressures

The two-dimensional model described earlier has three different domains - the aquifer, the matrix and the fracture blocks. A primary issue in the study was to determine the appropriate capillary pressure functions for the different domains.

For the aquifer blocks, since we wanted all of the liquid to be mobile we imposed zero capillary pressure. For the matrix blocks, the capillary pressure curves were similar to those derived from a typical Geysers isotherm (Satik et al., 1996), as described by the van Genuchten equation:

$$p_c = p_o\left(S_{ef}^{-1/\lambda} - 1\right)^{1-\lambda} \tag{2.2}$$

where p_o and λ are constants. S_{ef} is the effective liquid saturation given by

$$S_{ef} = \frac{S - S_r}{1 - s_r} \tag{2.3}$$

where S_r is the residual water saturation (Pruess et al., 1992). For the fracture blocks, we first thought that since the fracture has a large equivalent pore size, the capillary pressure would approach zero and hence would be independent of the saturation. Simulation runs were carried out using constant capillary pressures that ranged from 0 to 200 kPa for the fracture blocks. The simulation runs did not converge to a steady state solution. Hence, a linear capillary pressure function was used instead. A linear capillary pressure function was also utilized by Pruess (1985) and Hornbrook and Faulder (1993) for the fracture blocks in their studies.

2.3 THE EFFECT OF CAPILLARITY ON STABILITY AND FLUID FLOW BETWEEN THE FRACTURE AND THE MATRIX

It has been established in Section 2.2.2 that a water-saturated zone can remain stable over a liquid-dominated two-phase region. The question is, what would happen to this stability when a fracture is added to the system. Will the system become unstable and flip over? What role do capillary forces have on the observed stability? If the system is in fact stable even with the presence of the fracture, how do capillary forces affect the heat and mass transfer between the fracture and the matrix? These issues will be discussed in this section.

2.3.1 The two-dimensional models

The two-dimensional model constructed in Section 2.2.2 was utilized. The matrix and fracture properties are summarized in Table 2.2. There were five models used in this study, each differing in the type of capillary pressure function imposed on the fracture blocks.

Table **2.**2. **Parameters of the two-dimensional model used in the simulation.**

Property	Aquifer	Matrix	Fracture
Porosity	0.8	0.1	0.5
Permeability (md)	2000.0	0.5	50.0
Rock density (kg/m^3)	2643	2643	2643
Rock conductivity (W/m-°C)	2.88	2.88	2.88
Rock specific heat (kJ/kg-°C)	1.0718	1.0718	1.0718
Heat flux (W/m^2) - blocks 201-220		1.0	1.0
Relative permeability	$k_{rl} = (S)^3$ $k_{rv} = (1\text{-}S)^3$	$k_{rl} = (S)^3$ $k_{rv} = (1\text{-}S)^3$	$k_{rl} = (S)^3$ $k_{rv} = (1\text{-}S)^3$

Table **2.**3. **The capillary pressures used for the different models.**

Model	Aquifer	Matrix	Fracture
I	0	$p_{cm} = 0$	$p_{cf} = 0$
II	0	$p_{cm} = 100\left(S^{-1/0.6} - 1\right)^{0.4}$	$p_{cf} = -200S + 200$
III	0	$p_{cm} = 100\left(S^{-1/0.6} - 1\right)^{0.4}$	$p_{cf} = -100S + 100$
IV	0	$p_{cm} = 100\left(S^{-1/0.6} - 1\right)^{0.4}$	$p_{cf} = -50S + 50$
V	0	$p_{cm} = 100\left(S^{-1/0.6} - 1\right)^{0.4}$	$p_{cf} = 0$

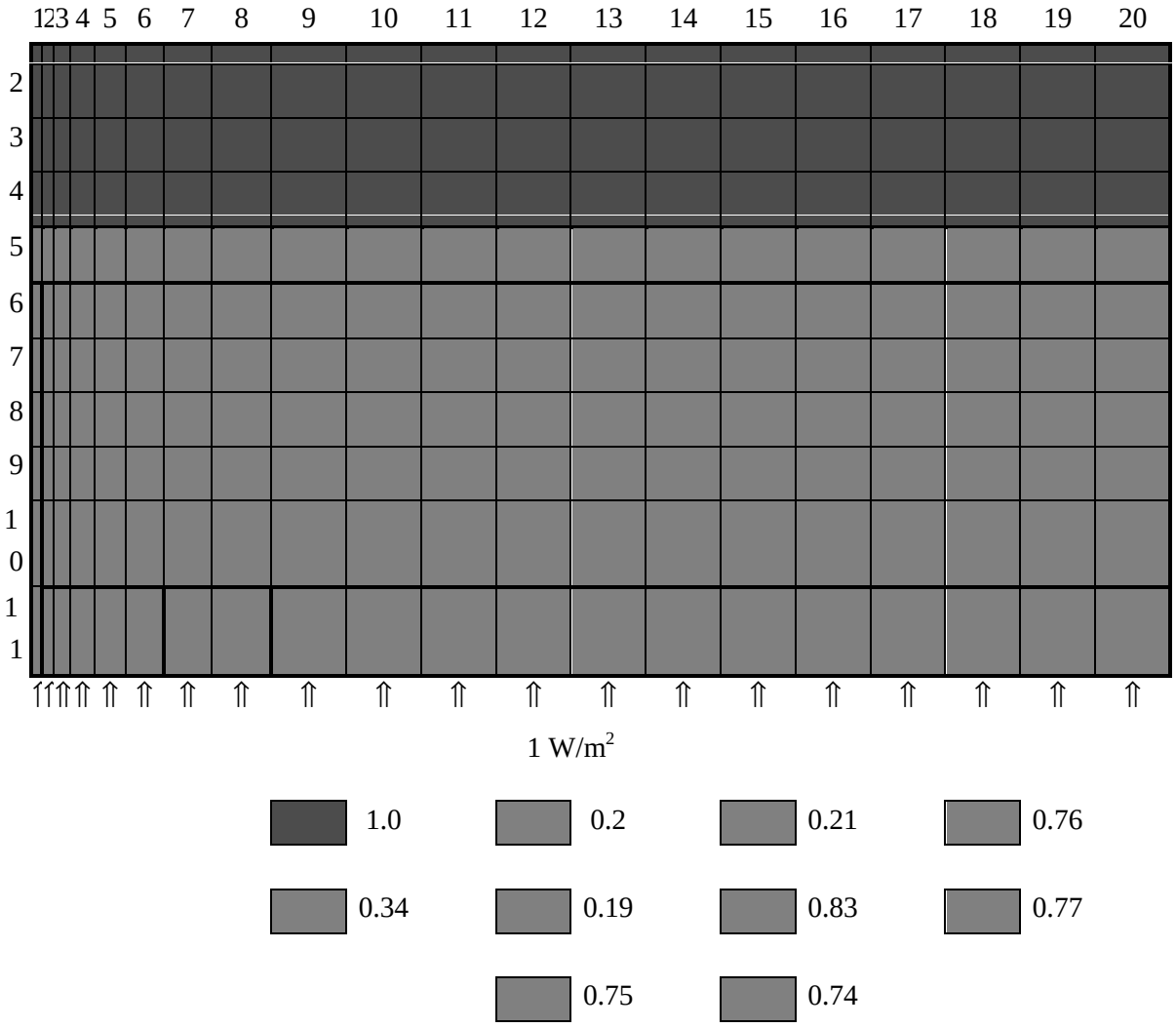

Fig. **2.**6. **Liquid saturation distribution for Model III.**

The matrix capillary pressure is described by the equation

$$p_c = 100\left(S^{-1/0.6} - 1\right)^{0.4} \qquad (2.4)$$

while the fracture capillary pressure is described by the equation

$$p_{cf} = -A(S) + A \qquad (2.5)$$

where S is the water saturation and A is the maximum fracture capillary pressure in kPa. There was no capillary pressure function assigned to the aquifer blocks. The capillary pressure functions used in the different models are shown in Table 2.3.

Using TETRAD version 12, simulations were carried out for up to 4 x 10^6 days in order to reach steady state.

2.3.2 Results and discussion

For Model I where no capillary pressures were prescribed, the two-phase region underneath the water-saturated zone collapsed. The temperature, pressure and saturation profiles indicate that we have a water-saturated region occupying the entire system.

For Model II where a van Genuchten type of capillary pressure curve was prescribed for the matrix blocks and a linear capillary pressure curve with a maximum value of 200 kPa was prescribed for the fracture blocks, an oscillatory behavior was observed for the temperature, pressure and saturation profiles with time. The period of oscillation was 3.5 cycles per 1 x 10^5 days.

For Model III where the maximum capillary pressure in the fracture blocks is 100 kPa, a water-saturated region remains stable on top of the two-phase zone. The saturation distribution is shown in Fig. 2.6. It was not unlikely that the fracture blocks, being highly permeable, would easily become saturated with water from the overlying four layers of fully water-saturated rock matrix. The numerical results obtained, however, indicate otherwise. In fact, the fracture has an average steam saturation of 80% while the adjacent matrix blocks are on the average 75% saturated with water.

The dimensionless heat flux for the fracture blocks in the two-phase region were calculated using Equation 2.1. These points when plotted versus saturation would lie towards the vapor-dominated heat pipe solution (Fig. 2.7). It can be noted that the point from Layer 5 is far from the analytical curve. This point actually belongs to the block that serves as an interface between the water-saturated and the vapor-dominated regions. Figure 2.7 indicates that the fracture blocks in Layers 6 to 11 form a vapor-dominated heat pipe.

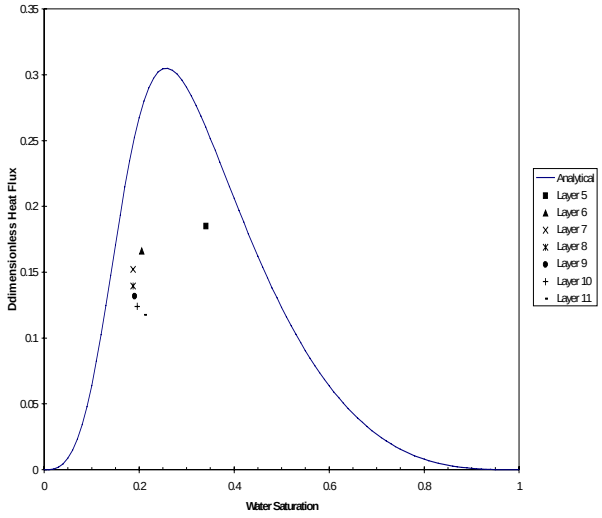

Fig. **2.**7. **Plot of the dimensionless heat flux versus saturation for the fracture blocks of Model III.**

For Model IV, the maximum capillary pressure in the fracture blocks was decreased by 50 kPa. The saturation field is shown in Fig. 2.8. When the maximum capillary pressure in the fracture blocks was

decreased to 50 kPa, the amount of water retained in the fracture blocks decreased. The average steam saturation in the fracture blocks within the two-phase zone was 85%. Correspondingly, the amount of fluid in the matrix blocks increased. The average water saturation in the matrix blocks became 93%. Calculations for the heat flux within the fracture blocks would indicate that we do have a vapor-dominated heat pipe (Fig. 2.9). The points are much nearer to the line representing the analytical solution.

The results from Model V show that the matrix blocks are almost entirely water-saturated (Fig. 2.11). Examination of the pressure, temperature and saturation distribution within the fracture blocks and the plot of the dimensionless flux versus saturation (Fig. 2.10) indicates that the fracture is actually a vapor-dominated heat pipe. When compared to Model IV, the saturations are not significantly different.

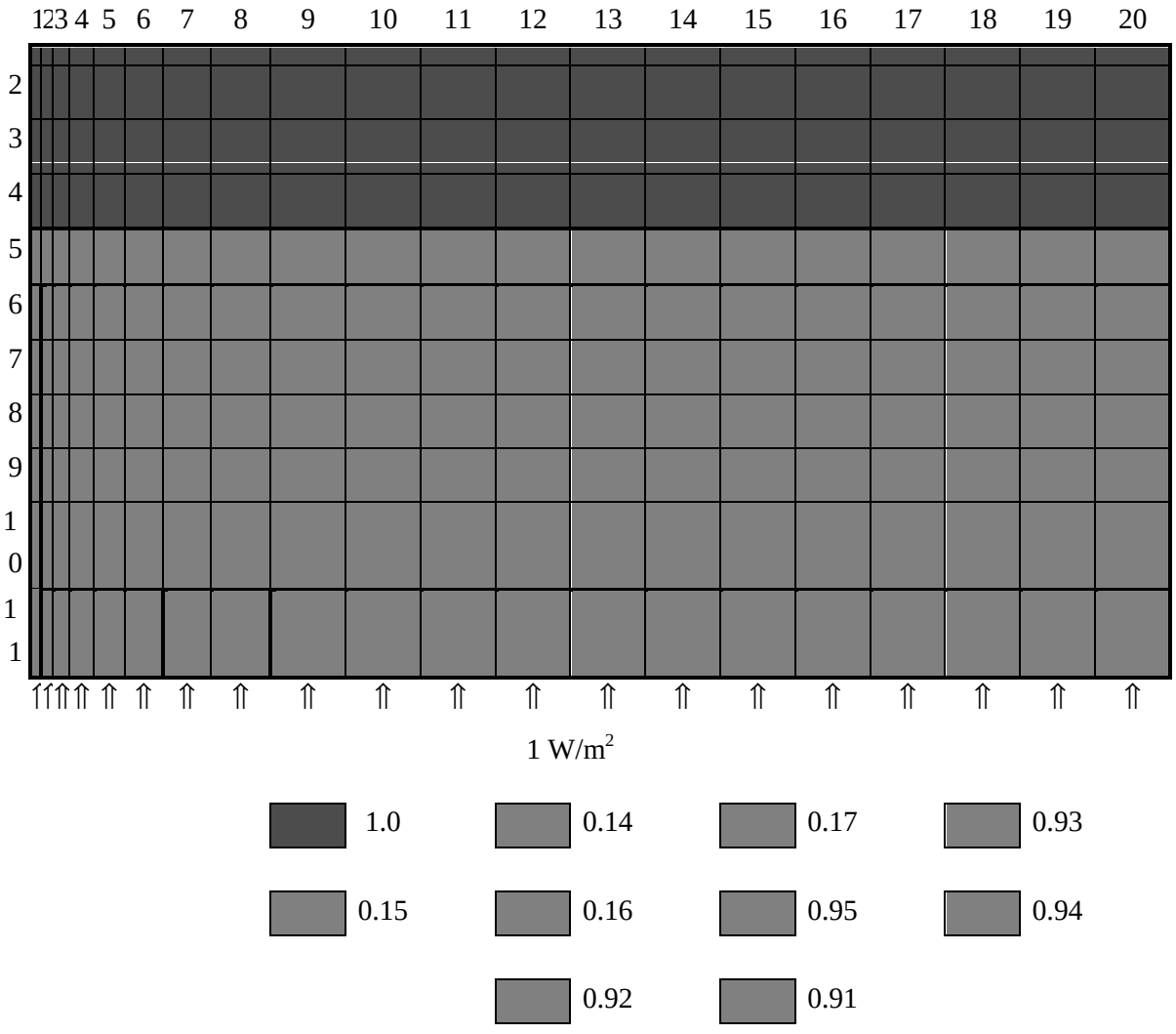

Fig. **2.**8. **Liquid saturation distribution for Model IV.**

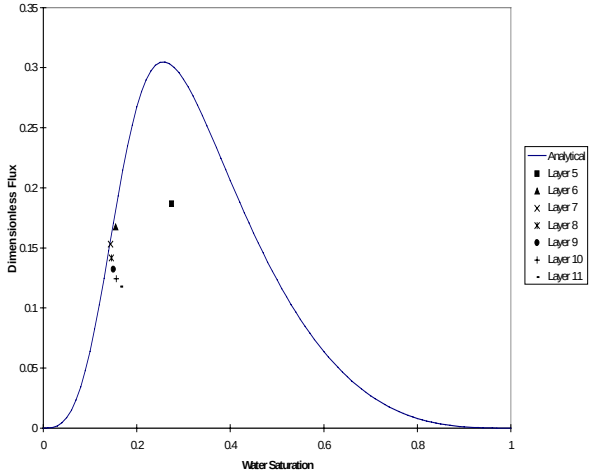

Fig. **2.**9. **Plot of the dimensionless heat flux versus saturation for the fracture blocks of Model IV.**

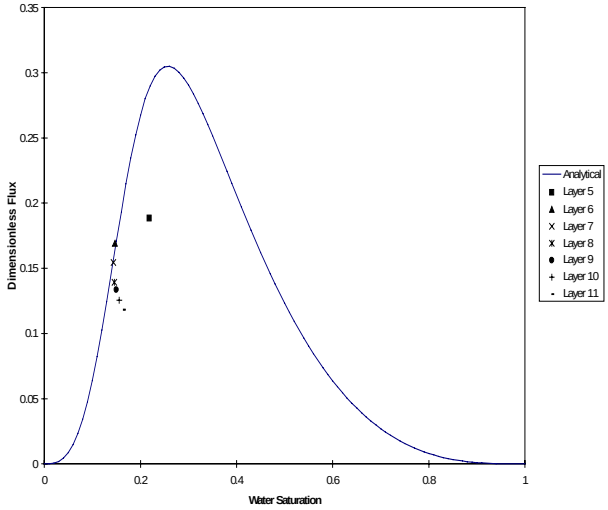

Fig. **2.**10. **Plot of the dimensionless heat flux versus saturation for the fracture blocks of Model V.**

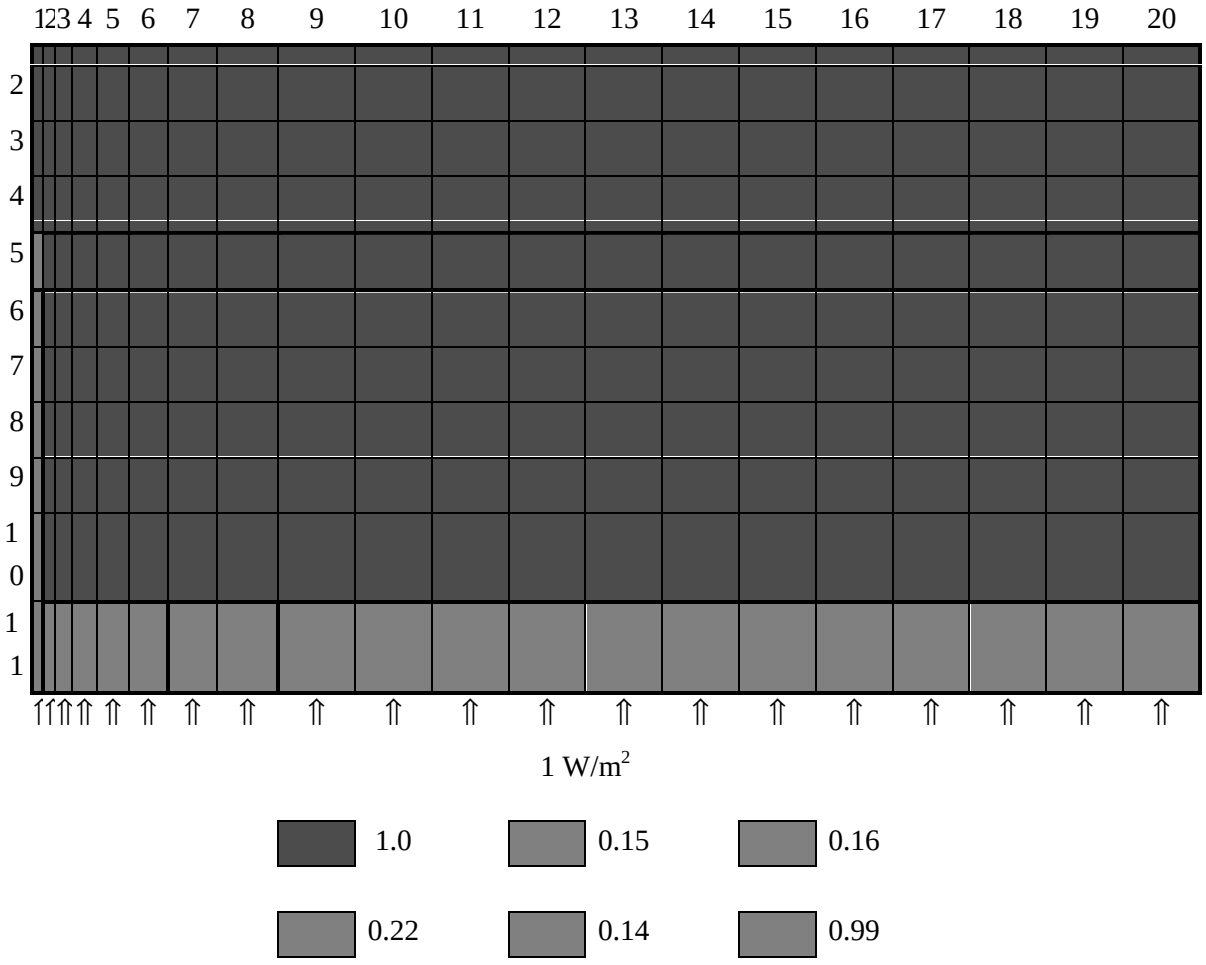

Fig. **2.**11**. Liquid saturation distribution for Model V.**

On the issue of stability, Model I indicates that numerically it is not possible to maintain a water-saturated region on top of a liquid-dominated two-phase fractured reservoir if no capillary pressure functions are specified for both the matrix and the fracture blocks. However, Model V gave the result that even if no capillary pressures were specified for the fracture blocks, a small two-phase zone could still exist below a water-saturated zone. Combining these observations, we can say that not specifying capillary pressures in the matrix blocks would destroy the stability of water over a liquid-dominated two-phase region.

From Models III to V, it can be observed that the fracture acted like a heat pipe and as the maximum capillary pressure specified on the fracture blocks is diminished, the average steam saturation increases. This is due to the fact that capillary forces tend to suck the liquid phase into the pores of the porous medium. In the presence of vapor, the capillary forces through adsorption would induce capillary condensation and the net effect is to have a higher liquid saturation. Not specifying capillary pressures in the fracture increases the heat pipe effect. This is good if we want to look at it in terms of heat transfer.

Heat is transmitted more effectively since the mode of heat transfer is through convection. Steam rises through the fractures and on reaching the water-saturated region, loses energy, condenses and trickles down. Liquid is also transferred from the matrix blocks into the fracture where it boils off and rises as steam. Numerical results indicate that as the capillary pressure in the fracture is diminished, the rate at which liquid is transferred from the matrix into the fracture is increased. Likewise, the steam flux going through the fracture is increased. In other words, convection is enhanced and so is heat transfer.

2.4 CONCLUSIONS

Capillary forces play an important role in determining the natural state of fractured geothermal reservoirs. Capillarity tends to keep the vapor phase in the fractures and the liquid phase in the matrix. In this manner, the fractures are not fully saturated with liquid and the possibility of having a heat pipe is increased. In Models III to V, the fractures were actually vapor-dominated heat pipes. Not having capillary pressure in the fracture blocks enhances the heat pipe effect, and also increases the transfer of liquid from the matrix into the fracture. Having low or no capillary pressure specified in the fracture blocks would improve the convection process and hence speed up heat transfer.

Based on the results obtained from Model II, it seems that the appropriate value for capillary pressures in fractures should not reach 200 kPa. This is reasonable due to the inverse relationship capillary pressure has with the mean pore radius. Since the mean pore radius is “large,” small capillary pressures are expected.

Capillary pressures are likewise important as far as the stability of a water-saturated region on top of a liquid-dominated two-phase zone is concerned. Not specifying a matrix capillary pressure (Model I) will cause the two-phase zone to collapse under the water-saturated zone.

The two-dimensional fractured model demonstrates that due to capillary forces, a liquid-dominated two-phase zone will remain stable under a water-saturated region. Normally, one would think that due to the presence of a high permeability conduit, the liquid would gush through the fracture and quench the two-phase zone, however, this is not necessarily the case.

The numerical stability of this system suggests that it is not necessary to model a geothermal system as having a caprock on top. This is the same observation made by Sondergeld and Turcotte (1977) based on their experimental results.

3. INFERRING INJECTION RETURNS FROM CHLORIDE MONITORING DATA

3.1 INTRODUCTION

Traditionally, tracer tests are used to establish the degree of connectivity between wells. However, for wells that are only weakly connected these tests may need to be conducted over long periods of time using huge amounts of tracer of sufficient stability to obtain meaningful data. In such cases tracer tests can be too costly and impractical.

On the other hand, there are substances occurring naturally in the reservoir that can behave as tracers. One such substance is chloride. In Palinpinon geothermal field in the Philippines, some injectors and producers are strongly connected so that changes in injection rates result in corresponding increase or decrease in chloride concentrations measured in production wells. Data from one such injector-producer pair in Palinpinon is shown in Fig. 3.1. The magnitude of the changes in chloride concentration thus reflects the degree of communication between wells. Moreover, chloride is stable, reasonably conservative and it is free. Therefore we may be able to extract the same, if not more, information from chloride data as we could from traditional tracer tests and at lower cost.

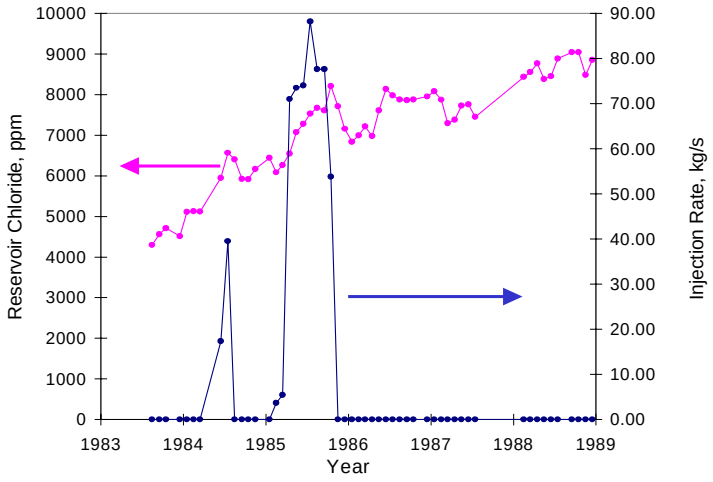

Figure 3.1: Example chloride and injection data from Palinpinon-I.

The following sections summarize how the method of wavelets and multiple regression techniques were used to analyze chloride and injection data and consequently, identify injection return flow paths; and, how the permeability of these paths were ranked by quantifying the degree of connectivity between injectors and producers.

3.2 PRELIMINARY LINEAR MODELS

As part of an optimization problem, an earlier work by Macario (1991) proposed several correlations for modeling the reservoir chloride and applied these models to data from Palinpinon-I geothermal field

in the Philippines. Of the models tested by Macario (1991), the linear combination model came closest to reproducing field observations. In the first phase of this project therefore, we chose to expand on that model and test it further.

Following is the original linear combination model proposed by Macario (1991):

$$Cl_p = a_0 + a_1 Q_{I1} + a_2 Q_{I2} + a_3 Q_{I3} + \ldots\ldots + a_n Q_{In} \quad (3.1)$$

Based on this model, the strength of the connection between the modeled producer P and an injector I_i is assessed by the magnitude of the coefficient, a_i, of that injector in the model; high values of a correspond to strong connections.

Aside from the extent of reinjection fluid returns, other factors could also affect the chloride level in the reservoir. Extensive boiling and steam separation within the reservoir and natural recharge of higher mineralized fluid are processes that could increase chloride concentrations (Harper and Jordan, 1985). The first process, boiling and steam separation, is a natural reservoir response to exploitation. The chloride concentration may therefore be expected to increase with time as the reservoir is produced. To model this variation with time, a linear time term was added to model (1), thus:

$$Cl_p = a_0 + a_1 Q_{I1} + a_2 Q_{I2} + a_3 Q_{I3} + \ldots\ldots + a_n Q_{In} + bt \quad (3.2)$$

More than anything, it was simplicity that guided our choice of the form (linear) of the time term. Solution saturation limits could be expected to put a cap on the maximum chloride concentration and cause it to level off late in the life of the reservoir. For practical purposes, however, we assumed that the chloride concentrations being modeled were far from the maximum limit and increased linearly with time. The question of how chloride concentration in the reservoir actually varies with respect to time will be addressed in more detail in a later section.

We also hypothesized that the reinjection returns' effect on reservoir chloride is governed not just by the rates of injection but also by the chloride concentration of the reinjected fluid. Hence, we have proposed the following modification to model (2):

$$Cl_p = a_0 + a_1 Q_{I1} Cl_{I1} + a_2 Q_{I2} Cl_{I2} + a_3 Q_{I3} Cl_{I3} + \ldots\ldots + a_n Q_{In} Cl_{In} + bt \quad (3.3)$$

The additional parameter Cl_{In} refers to the chloride concentration of the fluid being injected to injector I_n.

Results and Discussion

The original and extended models were applied to analysis of both the data set from Palinpinon-I previously used by Macario (1991) and another data set from the Dixie Valley field in Nevada. Qualities of the fit to the data were assessed by inspecting both the calculated values of the multiple regression coefficient, R^2, and plots of model predicted chlorides against actual data. The multiple regression coefficient, R^2, represents the proportion of variation in the modeled variable (in this case, chloride concentration) that is predictable from the model. It is therefore desirable to have high values of R^2. Only

the model which best fitted the data or equivalently, had the highest value of R^2 was subjected to further tests.

For any model to be considered relevant it was deemed necessary that that model be able to account for variations in chloride at any time interval in the data set regardless of which portion of the data set was used to calculate the linear coefficients. Thus we assessed model relevance by examining how well the model predicts later chloride measurements using coefficients that were calculated from earlier portions of the data set.

The following section discusses the results of application of models (1), (2), and (3) to the Dixie Valley and Palinpinon-I data sets. Model (3) was not used to analyze the Palinpinon-I data set due to the lack of injectate chloride data from that field.

Dixie Valley Case

At Dixie Valley, injection rates were recorded daily while chloride concentrations were measured much less frequently, thus, it was the amount of chloride data that set the limit to the number of data points (cases in which chloride concentrations and injection rates were available simultaneously) used for regression.

Table 3.1 lists R^2 values for models (1), (2), and (3) obtained for each production well. Except for wells 27-33 and 28-33, model (2) gave the highest value of R^2 for all production wells. Addition of the time term to model (1) resulted in 2 to 35% increase in R^2 while inclusion of injectate chloride concentration in model (3) did not result in any significant change in R^2 values. Figure 3.2 shows the effect of a 35% difference in R^2 on the quality of data fit for well 84-7; also, it illustrates the very minor effect that the injectate chloride term had on the quality of the match. Based on these results we chose to subject model (2) to further testing.

Table 3.1: R^2 values for Dixie Valley wells.

	R^2		
Well Name	Model (2.1)	Model (2.2)	Model (2.3)
27-33	0.917	0.963	0.965
28-33	0.852	0.936	0.940
45-33	0.935	0.970	0.966
63-7	0.826	0.828	0.815
73-7	0.774	0.952	0.952
74-7	0.755	0.968	0.967
76-7	0.930	0.947	0.943
82-7	0.764	0.969	0.967
84-7	0.716	0.978	0.978

Subsequently, the last six data points were excluded from the regression. Model (2) was then used to predict these values using the coefficients calculated based on the truncated data set. Fig. 3.3 plots the results of the truncated series analysis for well 27-33 which had a 9% maximum deviation of predicted

chloride from actual data - the highest deviation observed among all the production wells. Other wells had as little as 1% deviation (Fig. 3.4).

Inspection of the calculated coefficients revealed one possible reason for the relatively good predictive capacity displayed by model (2) (see Table 3.2). For this data set, the time term dominates the correlation; the coefficient of the time term is several orders of magnitude (three to five, even eight times!) greater than the injection rate coefficients. This discrepancy was enough to render the injection rate terms trivial: excluding an injection rate term from model (2) resulted in only tiny changes in the quality of the data fit. Fig. 3.5 shows the chloride match for well 74-7 when the chloride is predicted using model (2) but with injection rate term corresponding to injector INJ5218 excluded. That the injection rate terms are inconsequential to chloride prediction was also evident from inspection of the chloride data: for the most part, the chloride increased linearly with time and response to changes in injection rates was not readily evident. Hence, once the variation of chloride with time was captured in the analysis of the early portion of the data set and there was little deviation observed in the succeeding predictions. It was noted however, that although the deviations were small some of them showed a tendency to increase (Fig. 3.3). This was true for wells whose chloride ceased at some point to vary linearly with time.

At this point, it is worthwhile to recall that the goal of this project was not prediction but rather, correlation. Although for this specific data set model (2) matched and predicted chloride data relatively well, the dominance of the time term rendered the injection rate coefficients meaningless and ultimately made this model unsuitable for comparing the effects of injection wells on production wells in the field being considered here.

The preceding results lead us to conclude that for the purpose we have set for this project, multiple regression is not a suitable analysis tool for chloride data sets which lack texture.

Palinpinon-I Case

In this case, injection rate data were available as monthly average values; thus, chloride data were converted to monthly average values prior to analysis. As with the Dixie Valley data set, the amount of chloride data set the limit on the number of data points used for regression. Only the portion of the data set from 1983 to 1989 was initially available for use in the initial inspection of the linear models; thus, the following results pertain to the analysis of that early portion of the data set.

The effect on R^2 of adding the time term to model (1) was even more drastic for the Palinpinon-I data set: a maximum increase of 80% in R^2 was observed (Table 3.3) The effect of a 60% increase in R^2 on the quality of the match for well PN-16D is shown in Fig. 3.6.

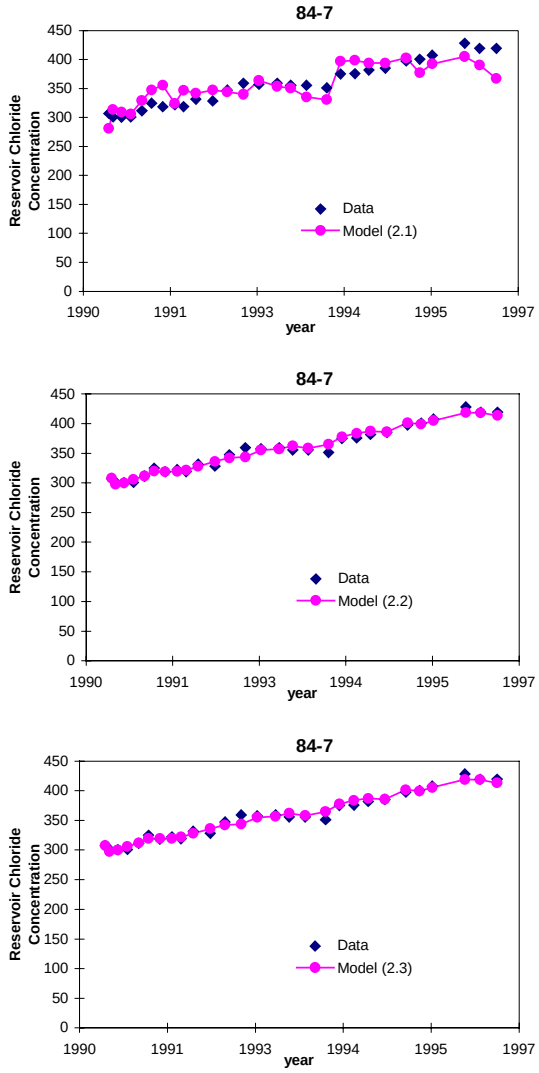

Figure 3.2: Predicted vs. measured chloride concentration for well 84-7, Dixie Valley.

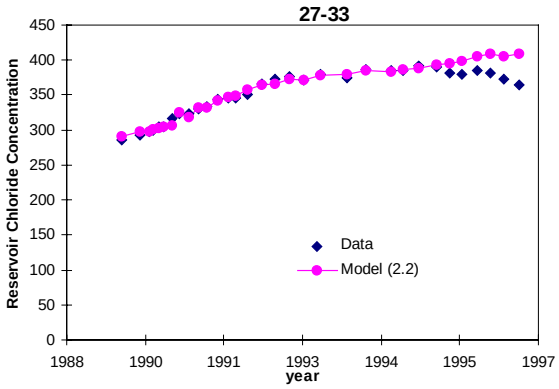

Figure 3.3: Predicted vs. measured chloride concentration for well 27-33, Dixie Valley; model (2) coefficients calculated with last six data points excluded.

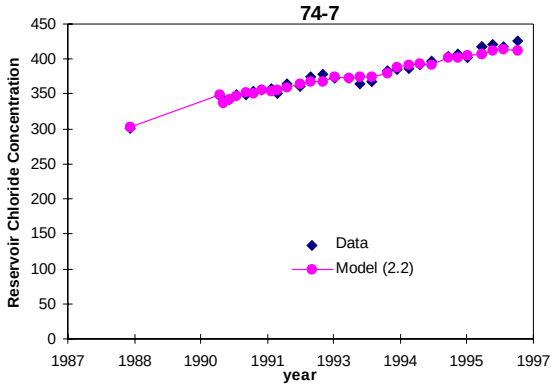

Figure 3.4: Predicted vs. measured chloride concentration for well 74-7, Dixie Valley; model (2) coefficients calculated with last six data points excluded.

Table 3.2: Model (2) coefficients for Dixie Valley production wells.

Model Parameter	Production Wells								
	27-33	28-33	45-33	63-7	73-7	74-7	76-7	82-7	84-7
a_0	314.58	354.39	271.46	283.77	272.43	318.32	384.12	254.39	271.60
Injection wells:									
INJ255	-6.61E-05	-4.84E-04	5.06E-04	1.80E-03	2.94E-04	1.51E-05	3.60E-04	-3.05E-06	3.99E-04
INJ455	-2.20E-04	-5.56E-04	3.33E-04	1.33E-03	2.70E-04	-1.62E-04	-1.37E-04	7.57E-05	3.89E-05
INJ3218	-1.21E-03	-4.30E-04	-1.54E-03	2.69E-03	2.12E-04	-5.89E-04	-3.59E-04	6.67E-04	-1.24E-03
INJ4118	4.58E-04	6.02E-04	3.54E-04	-4.40E-04	4.35E-05	7.31E-05	2.87E-04	-2.31E-04	9.76E-07
INJ5218	-1.20E-03	-7.39E-04	-1.18E-03	-2.95E-04	4.37E-04	-2.50E-04	-5.42E-04	7.43E-04	-1.42E-04
INJ6518	3.56E-03	3.40E-03	2.65E-03	-2.77E-03	-6.31E-04	9.02E-04	-5.63E-04	-3.33E-04	2.07E-03
INJ_SWL1	-3.99E-03	-3.74E-03	-3.33E-03	8.45E-04	5.39E-04	1.68E-04	4.18E-04	6.27E-04	-7.24E-04
INJ_SWL3	1.49E-03	9.69E-04	1.33E-03	-4.17E-03	-1.35E-03	-2.18E-04	-3.49E-05	-1.43E-03	-3.27E-04
t	8.48	10.37	7.61	2.30	17.44	12.95	4.82	26.25	19.04

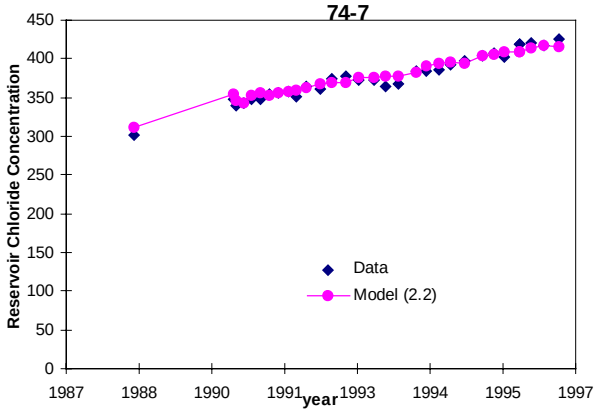

Figure 3.5: Predicted vs. measured chloride concentration for well 74-7, Dixie Valley; predicted values calculated using model (2) with one injection rate term excluded.

Table 3.3. R2 values for Palinpinon-I wells.

Well Name	R^2	
	Model (2.1)	Model (2.2)
OK-7D	0.783	0.956
OK-9D	0.717	0.902
OK-10D	0.490	0.535
PN-15D	0.824	0.993
PN-16D	0.606	0.964
PN-17D	0.519	0.939
PN-18D	0.718	0.930
PN-19D	0.559	0.903
PN-23D	0.736	0.958
PN-24D	0.706	0.895
PN-26D	0.728	0.922
PN-27D	0.696	0.944
PN-28D	0.643	0.895
PN-29D	0.817	0.948
PN-30D	0.710	0.832
PN-31D	0.625	0.946

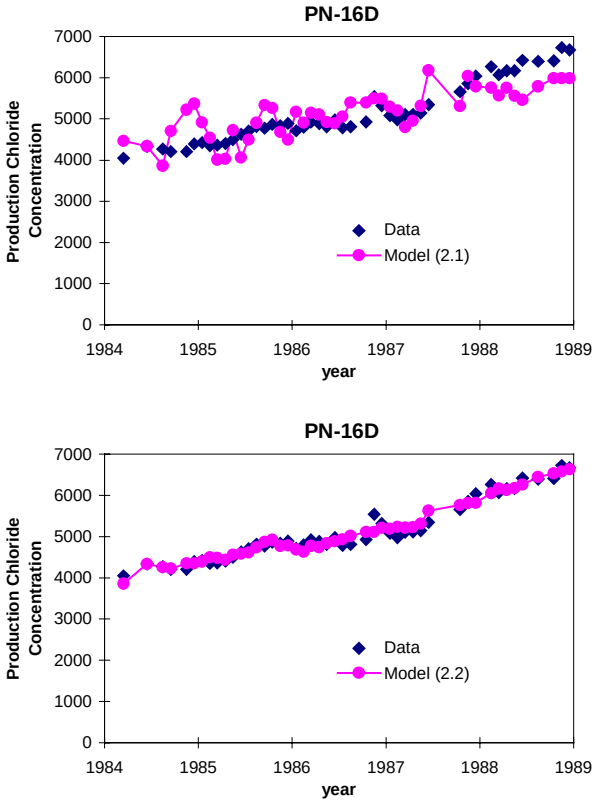

Figure 3.6: Predicted vs. measured chloride concentration for well PN-16D, Palinpinon-I.

As was done previously in the analysis of the Dixie Valley data set, in the subsequent regression using model (2) the last six points in the chloride series were not considered in the calculation of the linear coefficients. The excluded chloride values were then predicted using the coefficients calculated based on the truncated data set. Deviations of predicted chloride values from actual data for the Palinpinon-I data set were relatively high compared to those of Dixie Valley with a maximum of about 20%. Model (2) overpredicted the data for well OK-9D (Fig. 3.7) and underpredicted the chloride for well PN-19D (Fig. 3.8).

As with the Dixie Valley data set, the increasing deviations may be explained by the fact that the linear form of the time term does not account properly for the general trend in chloride with time. Moreover, the relatively high values of the deviations suggest that the injection rate terms contribute significantly to the model but that their contribution has not been assessed adequately.

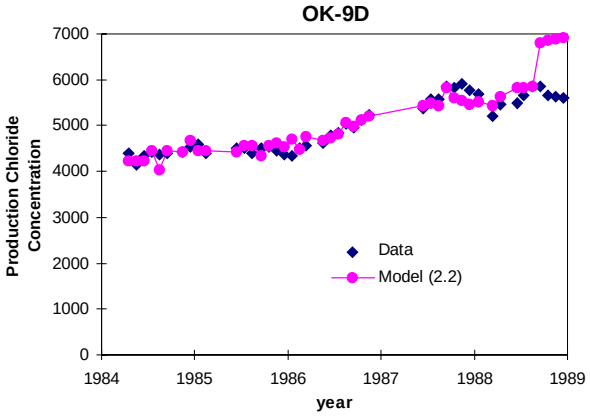

Figure 3.7: Predicted vs. measured chloride concentration for well OK-9D, Palinpinon-I; model (2) coefficients calculated with last six data points excluded.

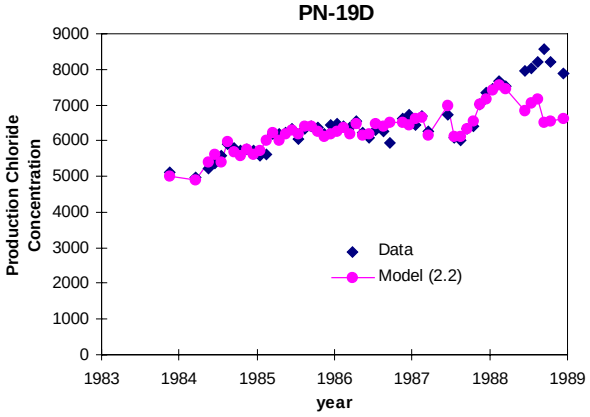

Figure 3.8: Predicted vs. measured chloride concentration for well PN-19D, Palinpinon-I; model (2) coefficients calculated with last six data points excluded.

Table 3.4 shows that the time term coefficients for this data set are only one to two orders of magnitude higher than the injection rate coefficients, as compared to five to eight orders of magnitude in the Dixie Valley data set. This is due to the more textured nature of the Palinpinon-I data; superimposed on the general increasing trend in chloride are marked dips and bumps. Since the dips and bumps which are accounted for by the injection rate terms are of substantial magnitude, the injection rate coefficients had high absolute values compared to those calculated for the relatively untextured Dixie Valley data set.

Table 3.4: Model (2) coefficients for Palinpinon-I production wells.

Model Parameter	Production Wells							
	OK-7D	OK-9D	OK-10D	PN-15D	PN-16D	PN-17D	PN-18D	PN-19D
a_0	5292.15	4290.85	3875.44	4761.51	3824.35	4917.71	4758.59	5043.93
Injection wells:								
PN-1RD	4.49E+00	1.15E+00	3.31E+00	2.56E+00	1.09E+00	1.04E+01	1.81E+00	-8.37E-01
PN-2RD	-2.49E+01	-7.06E+00	-2.27E+00	-7.73E+00	-5.82E-01	-1.13E+01	-2.27E+01	1.01E+00
PN-3RD	1.37E+00	5.97E+00	-2.64E+00	1.88E+00	-3.81E+00	-3.48E+01	-1.40E+00	-9.77E+00
PN-4RD	-1.75E+00	6.28E+00	9.97E-01	-1.63E+01	-5.25E-01	1.04E+00	-6.84E+00	-3.38E+00
PN-5RD	1.38E+01	-1.46E+01	-3.48E+00	1.01E+01	-4.68E-01	2.47E+01	7.15E+00	7.57E+00
PN-6RD	-4.51E+00	8.91E-01	3.62E+00	1.97E+00	-4.20E-01	2.72E+00	-1.75E+00	-4.68E+00
PN-7RD	5.69E+00	-5.69E+00	1.15E+01	1.67E+01	7.65E+00	9.72E+00	-4.55E+00	4.97E-01
PN-8RD	2.56E+00	-1.64E-01	6.77E-01	9.05E-01	2.36E+00	-1.49E+01	4.69E+00	4.92E+00
PN-9RD	1.07E+01	5.81E+00	-1.99E+00	-9.65E+00	9.92E-01	-1.04E+01	2.15E+00	-1.61E+00
t	683.31	322.12	123.82	707.56	590.02	881.05	670.13	621.24

Cont.

Model Parameter	Production Wells							
	PN-23D	PN-24D	PN-26D	PN-27D	PN-28D	PN-29D	PN-30D	PN-31D
a_0	4434.14	3770.09	5552.84	3949.51	5843.37	5233.71	4360.31	4365.67
Injection wells:								
PN-1RD	9.54E-02	-2.48E-01	7.56E+00	9.03E-01	6.16E+00	2.01E+00	-4.14E-01	1.33E+00
PN-2RD	-6.39E+00	-4.68E+00	-1.22E+01	-6.89E+00	-1.90E+01	-1.99E+01	-2.95E+00	2.01E-01
PN-3RD	4.71E+00	-5.60E+00	1.04E+00	1.54E+00	-1.06E+00	3.81E+00	3.96E+00	-2.84E+00
PN-4RD	3.02E+00	-7.31E+00	-1.15E+00	1.06E+01	-2.98E+00	-1.92E+00	8.92E-01	-5.57E+00
PN-5RD	-1.46E+00	2.85E+00	1.36E+01	-1.42E+01	5.99E+00	3.28E+00	3.24E+00	5.36E+00
PN-6RD	-1.92E+00	4.09E+00	4.53E-01	8.73E-01	-4.56E+00	-4.24E+00	-2.65E-01	-1.63E+00
PN-7RD	-3.10E+00	2.32E+01	6.82E+00	-5.24E+00	6.31E+00	-3.36E+00	-3.00E+00	-2.40E+00
PN-8RD	-1.86E+00	7.24E+00	3.87E+00	-6.15E-01	2.28E+00	1.31E+00	-3.07E+00	4.79E+00
PN-9RD	1.71E+00	9.74E+00	3.93E+00	1.11E+01	6.52E-01	9.01E+00	-1.15E-01	6.85E+00
t	475.82	661.45	685.95	569.91	708.20	836.91	189.52	677.22

It is also important to note that contrary to expectation, some of the injection rate coefficients had negative values. This implies that the operation of injection wells corresponding to those negative coefficients would actually lessen the percentage of injectate being produced. One explanation is that the injectors with negative coefficients could be diverting the flow from the other injectors away from the production well. It is also possible that increased injection to the well with negative coefficient prevents inflow of natural recharge fluids with higher chloride concentration.

Improvements

The linear form of the time term in model (2) was a very convenient assumption we made despite the nonlinear trend in chloride that was readily apparent from the data. Use of the linear time term in the previous section gave us an idea of how much the time variable accounted for variations in chloride. For both Dixie Valley and Palinpinon-I the previous results showed that the time term contributed a very significant part to the chloride model as implied by the high values of time term coefficients. From these observations came the motivation to set aside convenience and identify the correct form of the time term or equivalently the general trend in chloride with time. We have chosen to use wavelet analysis for this task.

Based on the results of our analysis of the Dixie Valley data set, we concluded that the effects of individual injection rate terms on chloride were trivial because their corresponding coefficients were very small compared to the coefficient of the time term. But is the significance of a variable's contribution to the regression solution really reflected by the magnitude of its coefficient in the regression equation? Would the comparison of those small coefficients from Dixie Valley result in as meaningful and valid conclusions as those derived from comparison of the bigger coefficients in Palinpinon-I?

Regression using model (2) gave us R^2 values that are very close to unity, signifying that the variation in chloride is almost entirely predictable from the model. Ironically, we also obtained regression coefficients that could not be generalized from the early to the later portion of the data set; that is, we observed poor predictive capacity of the model. How could we reconcile these results?

To answer these questions we turned to statistics and the next section outlines our findings.

3.3 MULTIPLE REGRESSION

The high values of R^2 coupled with poor predictive capacity observed in the previous chapter lead us to doubt the validity of the results of the previous regression work. A survey of materials/texts on multivariate statistics suggested that what we had was a case of overfitting: we had a solution that provided a wonderful fit to the sample (the early portion of the data set) but did not generalize to the population (the entire chloride series). According to Tabachnik (1996) overfitting is a result of having a sample size that is too small relative to the number of variables in the linear model. To illustrate the point, let us take the case of bivariate regression where a straight line ($y = mx + b$) is fitted through the data points available. When calculating the parameters m and b, the square of the prediction error (graphically, the deviation of the data points from the 'best fit' line) is minimized. In the extreme case where only two data points are available, the minimization problem reduces to a deterministic problem; m and b are calculated exactly based on the two data points and the solution becomes perfect (and meaningless).

Tabachnick (1996) suggests the following rules of thumb for the required sample size for multiple regression:

$N \geq 50 + 8m$ *for testing* R^2

$N \geq 104 + m$ *for testing individual coefficients*

Tables 3.5 and 3.6 show that for both Dixie Valley and Palinpinon-I the number of data points used in the previous regression analysis was significantly below the required amount of data suggested by Tabachnick (1996). This asserts that the R^2 values and coefficients calculated previously were only artifacts of the data analyzed and do not generalize to extensions of the chloride series. The restriction on the amount of data required for analysis prevented us from using the Dixie Valley data set. Fortunately, however a larger data set from Palinpinon-I was made available to us by PNOC-EDC and we used this extended data set for succeeding analyses. In instances where even the extended data set was short of the required amount of data, the only possible solution was to reduce the number of terms in the model to include only those which contribute significantly to the regression solution. The procedure for choosing the important terms is discussed later in this section.

Table 3.5: Number of data points in Dixie Valley data set.

	m = 9, model (2.2)		
Well Name	actual N	$(50 + 8m)$	$(104 + m)$
27-33	32	122	113
28-33	31	122	113
45-33	36	122	113
63-7	44	122	113
73-7	39	122	113
74-7	31	122	113
76-7	56	122	113
82-7	42	122	113
84-7	28	122	113

Table 3.6: Number of data points in Palinpinon-I data set.

	m = 10, model (2.2)		
Well Name	actual N	$(50 + 8m)$	$(104 + m)$
OK-7D	53	130	114
OK-9D	44	130	114
OK-10D	55	130	114
PN-15D	25	130	114
PN-16D	47	130	114
PN-17D	24	130	114
PN-18D	46	130	114
PN-19D	52	130	114
PN-23D	54	130	114
PN-24D	30	130	114
PN-26D	37	130	114
PN-27D	37	130	114
PN-28D	36	130	114
PN-29D	54	130	114
PN-30D	52	130	114
PN-31D	50	130	114

It is worth noting here that the addition of the time term to model (1) pushed the regression problem towards the deterministic region as it lowered the data-to-parameter ratio; hence, the increase in R^2 values observed previously.

Another issue raised earlier was that of the suitability of inferring the contribution of injection rate terms to the regression solution from the sizes of the coefficients alone. According to Tabachnick (1996), interpretation of the multivariate solution based on the sizes of the coefficients alone is strictly possible only in the case where all the independent variables or IVs (injection rates and time in the case of model 2) are indeed independent from each other. Disregarding the interdependence between IVs, there are statistical tests that allow us to tell whether the unique contribution of an IV as represented by its coefficient is significantly different from zero or not; that is, it tells one whether to accept or reject the hypothesis that the coefficient of an IV is zero. One such test is the probability or P-test. According to this test, there is a (100-*x*)% probability that an IV is important to the regression solution or equivalently, its coefficient is not equal to zero if its P-value is less than or equal to *x*%. It is common practice to set *x* to 5%; hence, there is a 95% certainty that the coefficient of an IV is not equal to zero if its P-value is less than or equal to 0.05. Calculation of P-values is discussed by Bowerman and O'Connell (1990) and is done automatically by the Microsoft Excel regression macro that we used. Note again that the P-test does not take into account the interdependence between IVs.

Considering the need to eliminate unimportant terms in the linear model to meet the data requirement as discussed previously and taking care not to exclude IVs whose importance are masked by their interdependence with other IVs, we have proposed the following procedure for succeeding application of multiple regression analysis:

1. To economize on IVs, temporarily set aside variables with P-values higher than 0.05;
2. Also, eliminate IVs with P-values lower than 0.05 and low values of simple correlation, *r*;
3. Inspect IVs which were eliminated in step 1 and put those with high *r* back to the model;
4. Perform another regression using the reduced model and interpret the results of this regression.

There are several possible variations to the preceding procedure and the one outlined above may not be the best but the important point to consider is the need to be aware of the possible complications that prevent straightforward interpretation of regression results based on the magnitude of coefficients alone.

3.4 WAVELET ANALYSIS

Recent work on the use of wavelet analysis (Jansen and Kelkar, 1997) in analyzing production data from oil fields prompted us to look into its applicability to our problem. In the course of our investigation we found out that wavelet analysis had a capability that serves our purpose of isolating the general trend of a signal (in our case, chloride concentration and injection rate) from its short-term variations. Wavelet analysis allows us to examine features of a signal of any size by decomposing the signal to different *detail* levels and a coarse *approximation.* The *approximation* retains the general trend with time while the details bear information on the signal's fluctuations at different time scales. Fig. 3.9 illustrates the concept using the chloride concentration signal from well OK-7D from Palinpinon-I. It is

worth emphasizing that the approximation to OK-7D chloride shown in Fig. 3.9 demonstrates that the general trend in chloride is nonlinear, contrary to the assumption in model (2).

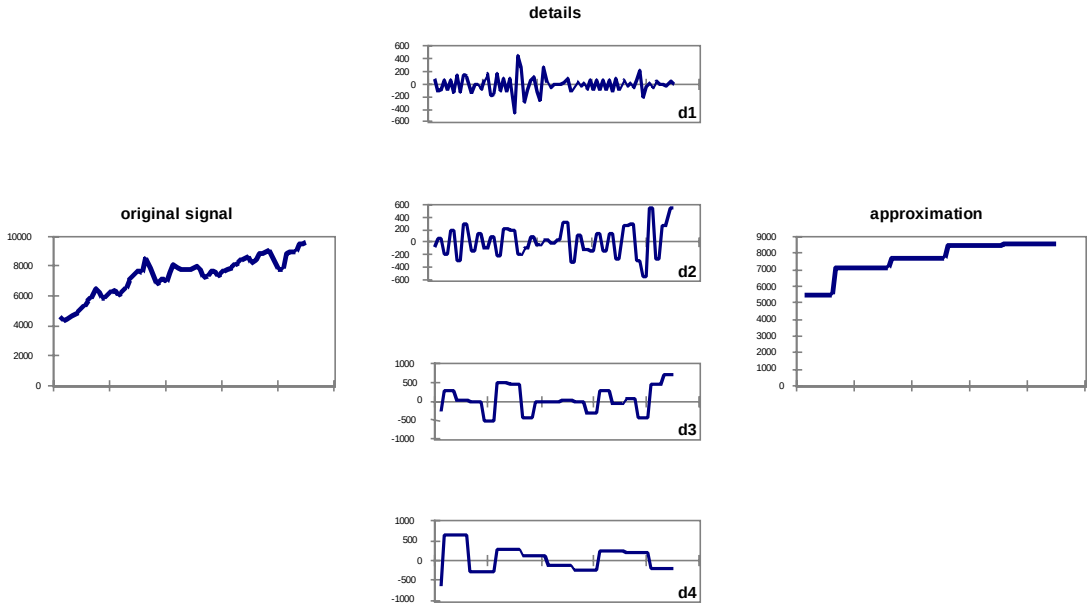

Figure 3.9: Wavelet decomposition: breaking a function down into a very coarse approximation, with an ordered sequence of detail functions making up the difference. (Chloride concentration, well OK-7D).

Since the effect of changes in injection rates is expected to manifest as short-term variations in reservoir chloride concentrations, it is more appropriate to analyze the *detail* functions described in the previous chapter instead of the *approximation* functions. Also, because the approximation functions isolate and retain the general trend in chloride with time, multiple regression of the details does not require a time term in the linear model. Thus, we used the following model:

$$Cl_p = a_1 Q_{I1} + a_2 Q_{I2} + a_3 Q_{I3} + \ldots \quad \ldots + a_n Q_{In} \qquad (3.5)$$

where Cl_p = chloride concentration detail in production well, P, Q_{In} = injection rate detail in injection well I_n, a_n = linear coefficient of well I_n

Comparison of coefficients obtained by using model (5) allows us to differentiate the degree of connectivity of different injectors to a given producer. Since details are deviations from local averages multiple regression using details ignores the differences in base chloride levels between producers. Regression results for different producers may therefore be intercorrelated; more specifically, the coefficients obtained may be used to compare the contributions of an injector to different production wells and consequently, to verify any conclusions drawn from the analysis against tracer test results.

The choice of modeling details over approximations was an obvious and straightforward decision. The appropriate detail level to model was less obvious, however. It seemed reasonable at first to assume that the best choice is the one that will give the highest R^2 value. Investigation of the R^2 values obtained from modeling the chloride details of OK-7D invalidated that assumption. Table 3.7 shows that at level 4 the regression coefficient becomes unity signifying a perfect correlation; and, correlation at succeeding

levels remain perfect. As the decomposition level goes up, the detail will have longer time intervals with constant values. This effectively reduces the amount of data to be modeled and results to a perfect, meaningless correlation. The choice is thus narrowed down to levels 1, 2, and 3.

Table 3.7: R^2 values for multiple regression of OK-7D chloride detail.

Detail Level	R^2
1	0.202
2	0.530
3	0.853
4	1.000
5	1.000

Inspection of injection and chloride details showed that the correspondence between changes in chloride concentration and changes in injection rate is more readily visible at level 3. In Fig. 3.10 the level 3 details of injection wells PN-6RD and PN-9RD closely follow the detail of OK-7D chloride during intervals when injection to these wells are high. Some degree of correspondence at levels 1 and 2 is also apparent from Fig. 3.11 albeit not quite as obviously as in level 3. Thus, we have decided to analyze all three levels of detail.

As was done in previous analyses, the chloride data that were recorded at irregular time intervals were converted to monthly average values to put them in the same time basis as the injection rates. Since wavelet analysis requires that data be available in the entire time interval being analyzed, missing chloride data were linearly interpolated. Interpolation was done over maximum intervals of six months and only when no drastic fluctuations were apparent within six months of the interval where interpolation was to be done. Where interpolation was not possible, we analyzed only the longest continuous portion of the data series.

When taking wavelet transforms of discrete data, the algorithms used require that the data set size be a power of two. A common way to precondition the data when this is not true is to "pad with zeroes," that is, to increase the size of the data set to the next larger power of two. Although this is a reasonable approach, it is problematic in that it "dilutes" the signal near the end of the original data set since wavelet coefficients will have zeroes averaged into their computation (Ogden, 1997). We believe that Matlab, the program we used to take the wavelet transform of our data, practices this data preprocessing procedure as evidenced by the inaccurate reconstruction near the end of the data series. It was therefore necessary to truncate the detail component functions used in regression analysis to eliminate the end effects of padding with zeroes. Plots of wavelet component functions retain the end effects but in the analysis, three to six data points were eliminated from the details series.

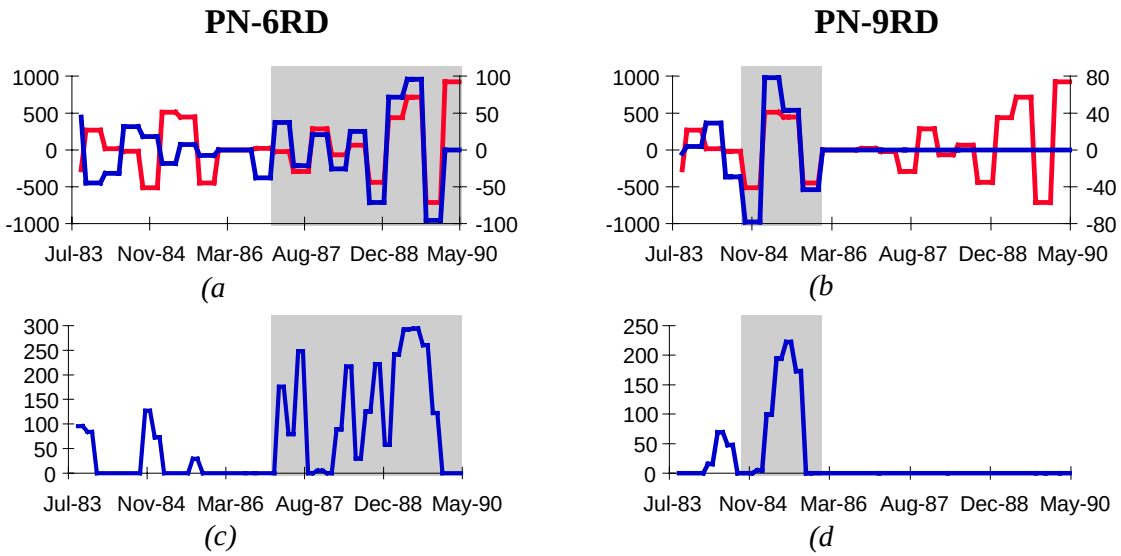

Figure 3.10: (a) Level 3 detail of OK-7D chloride - light line; level 3 detail of PN-6RD injection rate - dark line. (b) Level 3 detail of OK-7D chloride - light line; level 3 detail of PN-9RD injection rate - dark line. (c) PN-6RD injection rate. (d) PN-9RD injection rate.

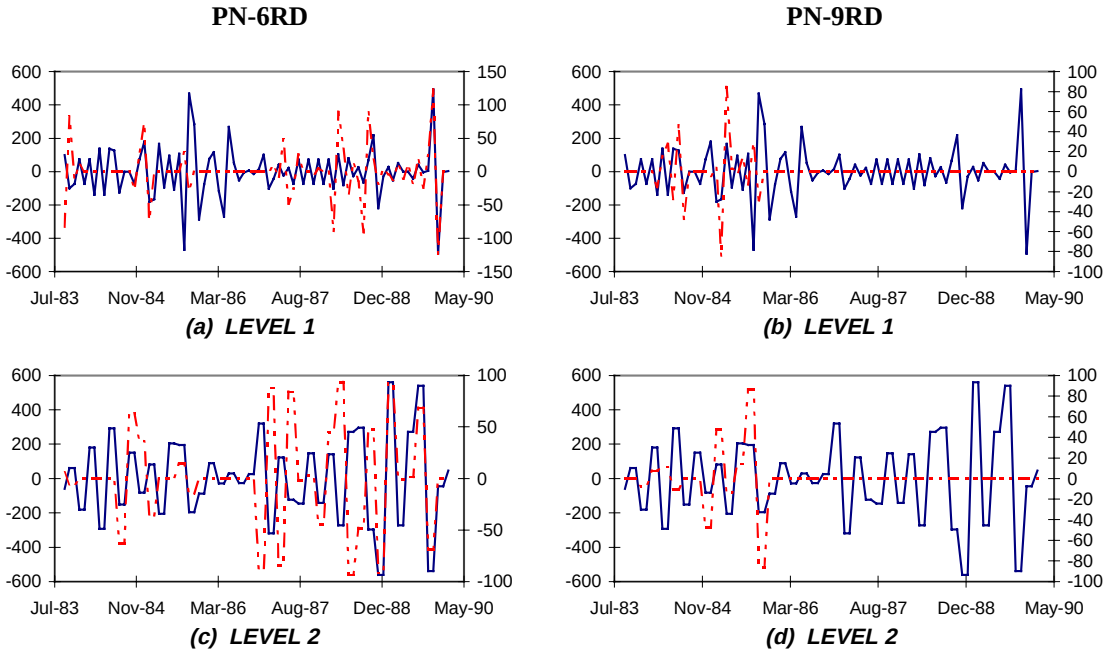

Figure 3.11: (a) Level 1 detail of OK-7D chloride - solid line; level 1 detail of PN-6RD injection rate -dashed line.

(b) Level 1 detail of OK-7D chloride - solid line; level 1 detail of PN-9RD injection rate - dashed line.

(c) Level 2 detail of OK-7D chloride - solid line; level 2 detail of PN-6RD injection rate -dashed line.

(d) Level 2 detail of OK-7D chloride - solid line; level 2 detail of PN-9RD injection rate - dashed line.

In about 1990, the bulk of the injection in Palinpinon-I was moved farther away from the production sector resulting in some injection wells being shut off and new ones being operated. Thus, based on operating time, injection wells in Palinpinon-I can be grouped into three: those which operated between 1983 and 1990, those which started to inject in 1990 and are still injecting, and those which have been injecting since 1983 and are still injecting. It is logical to assume that regression analysis will be best able to assess the degree of contribution of injection wells if all the wells are operating during the time interval over which the regression is done. So, where possible, the chloride series was divided into two time intervals, 1983 to 1990 and 1990 to present; and, regression analysis included only wells which were operating during those periods.

Regression was done for levels 1, 2, and 3 of the detail functions using the procedure outlined earlier. In some cases, that procedure had to be applied repeatedly until the number of terms left in the linear model is such that the data size requirement is met (or almost met). When eliminating injection well terms that had small *r* values, care was taken not to remove wells which operated only for very short periods of time (the small *r* values in these cases are unnatural effects of the scarcity of correlatable data).

Checking Results Against Tracer Test Data

Two sets of radioactive tracer test results were available for comparison with results of our analysis: that of the test conducted on well PN-9RD and one on OK-12RD. Both sets were reported by Macario (1991) and are reproduced in Table 3.8. Macario (1991) defined mean transit time as the time it takes for half of the tracer return to reach the production well. Assuming that the mean transit time measures the degree of connectivity between the injector tested and a producer (lower transit times corresponding to stronger connections) Table 3.8 lists the production wells in order of *decreasing* connectivity with the injector. Correspondingly, Tables 3.9 and 3.10 lists the wells affected by OK-12RD and PN-9RD, respectively, in the order of decreasing coefficients based on regression on all three wavelet detail levels.

Table 3.10 shows, with the exception of one well, that all wells affected by PN-9RD had positive coefficients. Comparison of Table 3.10 with Table 3.8 shows that tracer return was indeed monitored in all wells shown by regression analysis to be affected by well PN-9RD, including PN-29D which had a negative coefficient. More importantly it shows that the order of the strength of connection between PN-9RD and the wells monitored in the tracer test was most closely mimicked by the results of regression on detail level 3 with OK-7D showing the strongest connection to PN-9RD and PN-29D, PN-16D, and PN-23D displaying connections of about the same strength.

Table 3.8: Radioactive tracer test results for PN-9RD and OK-12RD.

Monitored Well*	Mean Transit Time, days
PN-9RD Tracer Test	
OK-7	5.4
PN-26	13
PN-28	14
PN-29D	15.4
PN-30D	15.7
PN-23	15.8
PN-16D	16
PN-19D	16
PN-31D	16
PN-18D	17.2
OK-9D	monitored, no return
OK-12RD Tracer Test	
PN-15D	7.3
OK-10D	13.8
OK-7D	14.6
PN-29D	monitored, no return

** Only wells which have chloride data are reported here.*

Table 3.9: Regression results for OK-12RD.

OK-12RD

Affected Well	Coefficient
d1	
OK-10D	12.38
d2	
PN-23D	2.46
PN-29D	-4.05
PN-31D	-10.82
d3	
PN-15D	125.27
PN-16D	-7.40
PN-29D	-3.34
PN-30D	6.15

Table 3.10: Regression results for PN-9RD.

PN-9RD

Affected Well	Coefficient
d1	
PN-30D	5.74
PN-29D	3.99
PN-16D	1.47
d2	
PN-19D	4.87
PN-18D	4.06
OK-7D	2.96
PN-16D	2.02
PN-29D	-11.65
d3	
OK-7D	9.40
PN-29D	1.83
PN-16D	0.92
PN-23D	0.43

On the other hand, comparison of Table 3.9 with Table 3.8 shows that tracer return was observed in two of the seven wells shown by regression analysis to be affected by well OK-12RD. Four of the seven wells were not monitored during the tracer test. As with PN-9RD, the well which is most connected to OK-12RD based on the tracer test had the highest coefficient at level 3 regression.

Based on these observations we have concluded that regression analysis of details at level 3 best assesses the degree of connectivity between wells: high positive coefficients correspond to strong connections and, negative and low positive coefficients correspond to weak connections.

Harper and Jordan (1985) reported the following observation: from May 1984 to October 1984 a large increase in reservoir chloride occurred in production wells PN-19D, 23D, 29D, 31D, OK-7D and OK-9D when reinjection was shifted to the wells PN-7RD and PN-8RD. This observation matches the results of level 3 detail analysis for well PN-8RD as outlined in Table 11: OK-7D, PN-19D, and PN-31D were all found to be strongly connected with PN-8RD. PN-23D, -29D, and OK-9D may have been receiving reinjection returns from OK-7D but no injection rate data from OK-7D was available to allow verification with regression results.

Table 3.11: Level 3 regression results for PN-8RD.

PN-8RD

Affected Well	Coefficient
d3	
OK-7D	3.14
PN-16D	0.64
PN-18D	2.76
PN-19D	4.93
PN-30D	-1.36
PN-31D	10.49

On the other hand, Amistoso and Orizonte (1997) reported that OK-10D and PN-20D experienced enhanced steam flows which they attributed to reinjection fluids intruding into the production sector at deeper levels. They cited the wells TC-2RD, TC-4RD, PN-3RD and PN-5RD to be wells that are providing pressure support to the reservoir due to deep injection but attributed the enhanced steam flow in OK-10D and PN-20D to TC-2RD and TC-4RD, specifically. Regression analysis results for these wells (Table 3.12), however, show that OK-10D is not affected by TC-2RD; rather it is affected by PN-1RD, PN-2RD, and PN-3RD between 1986 and 1990 and by PN-3RD, TC-3R, N3 and OK-3R between 1990 and 1996. It is worth noting that the effect of PN-3RD on OK-10D was found to be consistent between the intervals 1986-1990 and 1990-1996 as reflected by close *r* values for the two periods (-0.79 and -0.77). The large positive coefficient of well N3 is suspect however as it conflicts with its negative *r* value. PN-20D was also analyzed to be affected by PN-3RD. The effect of TC-2RD and TC-4RD on PN-20D could not be ascertained from regression analysis due to insufficient chloride data from PN-20D after 1990.

Pamatian (1997) reported that reinjection fluid from TC-2RD neutralized the fluid acidity in wells OK-10D and PN-13D. Again, the effect of TC-2RD on OK-10D was not substantiated by regression results but its effect on PN-13D was (Table 3.13). Again, terms with conflicting *r* and coefficient signs posed interpretation problems.

3.5 CONCLUSIONS AND RECOMMENDATIONS

Based on the results of regression analysis of chloride and injection rate data from Dixie Valley, we have concluded that multilinear modeling is not suitable for analyzing data sets which lack sufficient time variability or "texture".

A closer look at multiple regression techniques showed that what seemed to be highly encouraging results (high R^2 values) from prior multilinear modeling were but effects of the scarcity of data used in the correlation; hence, no meaningful physical interpretation may be drawn from them. Moreover, it showed that care should be taken not to base the interpretation of multiple regression results on straight-forward comparison of coefficients alone.

Wavelet analysis provided more useful results. Qualitative field observations and tracer test data agreed best with the results of regression on level 3 *detail* of chloride concentration and injection rates in Palinpinon-I: wells identified by tracer tests to be strongly connected had high positive coefficients and weak connections were indicated by negative and low positive coefficients at level 3 regression. This suggests that producer-injector interactions are best detected by correlating changes in chloride concentration over periods of four months (corresponding to level 3 resolution) with corresponding four-month fluctuations in injection rates. While the good correlation at such a relatively low level of time resolution may be explained as the result of the natural dispersion of chloride and injection rate signals as they propagate through the reservoir, it is also possible that this is due to the loss of information brought about by the use of monthly averaged data values in the analysis. It is therefore recommended that both chloride and injection rate data be recorded more frequently and the analysis be done on this larger data set. It is also possible that the Haar wavelet that was used in signal decomposition was too coarse in that it contributed to the loss of texture in the data. Investigation of the effects of using smoother wavelets is also recommended.

Table 3.12: Level 3 regression statistics for OK-10D and PN-20D.

OK-10D (1986-1990)

d3	
Regression Statistics	
Multiple R	0.839369312
R Square	0.704540842
Standard Error	79.20406691
Observations	48

	Coefficients	*r (simple)*	*Standard Error*	*t Stat*	*P-value*
pn1rd	1.0860989	0.742898166	0.432894148	2.508924886	0.01577982
pn2rd	-3.71087522	-0.72596153	1.775342121	-2.09023105	0.04227759
pn3rd	-4.4114713	-0.78948113	1.783793986	-2.4730834	0.01723762

OK-10D (1990-1996)

d3	
Regression Statistics	
Multiple R	0.835160095
R Square	0.697492385
Standard Error	150.1670809
Observations	80

	Coefficients	*r (simple)*	*Standard Error*	*t Stat*	*P-value*
pn3rd	-11.4979076	-0.77103302	1.485833395	-7.7383559	3.4832E-11
tc3r	1.704839524	0.522611064	0.404330736	4.216448003	6.7759E-05
n3	30.87773863	-0.65393407	6.498963063	4.751179278	9.3559E-06
ok3r	-7.36184797	-0.36088849	2.134566707	-3.44887229	0.00092135

PN-20D (1983-1989)*

d3	
Regression Statistics	
Multiple R	0.635764265
R Square	0.404196201
Standard Error	495.2038572
Observations	80

	Coefficients	*r (simple)*	*Standard Error*	*t Stat*	*P-value*
pn1rd	10.21445053	0.346132276	1.741845857	5.864152953	1.0654E-07
pn3rd	12.28448348	0.357197703	2.153358367	5.704802167	2.062E-07
pn6rd	4.493768629	0.105136293	1.637086662	2.744979074	0.00752785

**No chloride data was available from 1990 to 1993 and remaining data points were not sufficient for analysis.*

Table 3.13: Level 3 regression statistics for PN-13D.

PN-13D (1990-1996)

d3	
Regression Statistics	
Multiple R	0.962568329
R Square	0.926537788
Standard Error	74.57273176
Observations	70

	Coefficients	*r (simple)*	*Standard Error*	*t Stat*	*P-value*
tc2rd	4.826890146	0.403207897	0.459363951	10.5077687	1.4452E-15
tc3r	1.989170863	0.37912479	0.16882133	11.78269865	1.1114E-17
tc4r	52.80156771	-0.47305009	4.657792303	11.33617909	5.9844E-17
ml1rd	-191.386684	-0.73129226	16.95558741	-11.2875289	7.1995E-17
n3	11.67741779	-0.76944945	1.849731659	6.313033424	2.9328E-08
ok3r	27.49754181	-0.47241942	2.227450499	12.34484978	1.3816E-18

Emphasis is also placed on the need for continuous data measurements when doing wavelet analysis. Highly intermittent measurements result in data loss: since it is considered safe to interpolate only over short periods of time, the lack of data over long time intervals forces one to disregard the data collected prior to such periods when doing the analysis.

Another possible improvement to consider in future regression analyses is to take into account possible nonlinearity in the variation of chloride with injection rates. While nonlinearity does not invalidate the analysis, it certainly weakens it as the relationship between chloride concentration and injection rates is not completely captured by the coefficients of the linear model. Although regression analysis uses a linear model, effects of nonlinearity in the variation of chloride with injection rates may be incorporated into the model by using nonlinear terms: the model is kept linear even though the individual terms are not. Results of this modified analysis will be more difficult to interpret however, because the strength of interaction between producers and injectors will be measured not only by the magnitude of the coefficients but also by the exponent of each term.

3.6 NOMENCLATURE

a_0 = a constant associated with local initial chloride concentration
a_n = linear coefficient of well I_n
b = linear time term coefficient
Cl_{In} = chloride concentration in injector well, In
Cl_P = chloride concentration/chloride concentration detail in production well, P
m = number of predictors
N = number of data points
Q_{In} = mass flow rate/mass flow rate detail to injection well, In
r = simple regression coefficient
R^2 = multiple regression coefficient
S = standard deviation
SS_{reg} = sum of squared deviations of predicted Y from the mean
SS_Y = sum of squared deviations of Y from the mean
Y = dependent variable being modeled
Y' = predicted values of Y
$\overline{Y}$ = average value of Y

4. INFERRING RELATIVE PERMEABILITY FROM DYNAMIC BOILING EXPERIMENT

4.1 INTRODUCTION

Relative permeability is important in describing multiphase flow since it contains the information regarding movement of one phase with respect to another. It is given as a function of saturation, interfacial tension, wetting characteristics, and viscosity ratios. So far, relative permeability relations have been based on theoretical methods using field data, and laboratory experiments. Although relative permeability is best determined through laboratory experiments, it is difficult to measure due to capillary forces that introduce nonlinear effects on the pressure and saturation distribution at the core exit (Ambusso, 1996). In particular, the relative permeability is difficult to measure directly for steam-water flows mainly due to the heterogeneity of the core, equipment or material limitations (i.e. the need to withstand high temperatures and pressures), and inaccuracy of the experimental methods (Satik, 1997).

Recently, significant improvements were achieved in measuring saturations and collecting data from steam-water flow experiments. These results indicated a linear relationship for steam-water relative permeability (Ambusso, 1996). In attempting to repeat these results, Satik (1998) made a significant improvement in the design of the experimental apparatus. A successful experiment was conducted and steam-water relative permeability was obtained. These recent results suggest a curvilinear relationship that is different from the results obtained by Ambusso (1996) (linear relationship).

This paper describes a second approach to estimating the relative permeability by matching data from a boiling experiment with results obtained from numerical simulation. This method provides a way to examine the validity of the relative permeability measurements taken from previous experiments as well as to estimate capillary pressure since the parameters in the relative permeability and capillary functions used (Brooks-Corey functions) are interrelated.

4.2 EXPERIMENTAL APPARATUS

In the actual experiment (Fig. 4.1), a 43 cm long Berea sandstone core with radius 2.54 cm was sealed with epoxy and insulated with ceramic fiber blanket. The core was first saturated with liquid water and then heated at the bottom. Water was allowed to flow out from the top end of the core, which was maintained at atmospheric conditions. The heater was placed at the bottom of the core and insulated to minimize heat loss. During the vertical boiling experiment, temperature, water pressure, and heat flux values were measured at 41 points along the length of the core using thermocouples, pressure transducers, and heat flux sensors; while steam saturation was measured using a CT scanner. The power of the heater was increased nine times from 0.864 mW to 10.42 W. A detailed description of the experiment is given in Satik (1997). Table 4.1 shows the properties of the sandstone and materials used in the experiment.

4.3 MODEL

TOUGH2 is a multidimensional numerical model for simulating the transport of water, steam, air, and heat in porous and fractured media (Pruess, 1991). ITOUGH2 (Finsterle, 1997) provides inverse modeling capabilities for the TOUGH2 codes and solves the inverse problem by automatic model calibration based on the maximum likelihood approach. In this study, parameters were estimated based on temperature, water pressure, steam saturation, and heat flux for which a corresponding TOUGH2 output was already available, including initial guesses, for the parameters to be estimated.

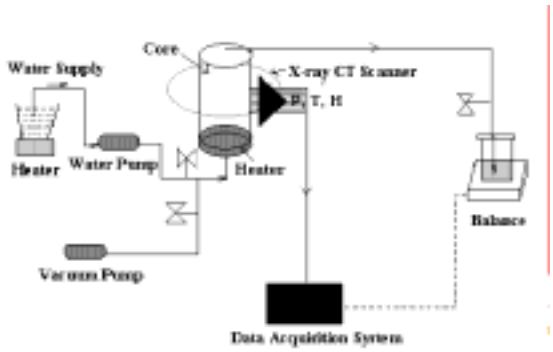

Figure 4.1: Schematic diagram of the experimental apparatus (from Satik, 1997).

Table 4.1: Properties of the materials used in the boiling experiment.

Material	ρ kg/m^3	k 10^{-13} m^2	ϕ %	α W/m-^{0}C	C J/kg-^{0}C
Berea	2163	8.487	22	4.326	858.2
Heater	2200			2.885	
Heater insul.	529			0.125	1046.6
Epoxy	1200			0.577	1046.6
Insulator	192			0.090	104.7

The TOUGH2 simulation grid used is a two-dimensional radial model with 3 rings and 51 layers (Figure 4.2). Except for the layers 45-51 (seven bottommost layers), the first (innermost) ring represents the core; the second ring represents the epoxy; and the third ring represents the insulator. The heater is located in the layer 45 in ring 1, and the heater grid block is further refined into five smaller grid blocks. Moreover, the heater insulator is in layers 46-51, rings 1-3. Rings 2-3 in layer 45 represent epoxy and core insulator, respectively. Constant pressure boundary conditions are applied to layer 1 (topmost layer) in ring 1. To simulate a constant pressure boundary, layer 1 grid blocks are assigned a much larger volume than the core layers. All grid blocks from layer 1 to layer 51 in ring 3 and layer 51 in rings 1-2 are attached to a large grid block that is under ambient conditions in order to model heat loss to the surroundings. Since

there is no fluid flow in the radial direction, non-zero permeability values are assigned only in the vertical directions.

4.4 MODIFIED BROOKS-COREY FUNCTIONS

The modified Brooks-Corey relative permeability functions are given as:

$$k_{rl} = S_{ek}^{(2-3\lambda)/\lambda} \quad (4.1)$$

$$k_{rg} = (1 - S_{ek})^2 (1 - S_{ek}^{(2-3\lambda)/\lambda}) \quad (4.2)$$

The modified Brooks-Corey capillary pressure functions are given as

$$p_c = -p_e \left[\varepsilon / (1 - S_{wr})\right]^{-1/\lambda} - (p_e / \lambda)\left[\varepsilon / (1 - S_{wr})^{(1-\lambda)/\lambda}\right](S_l - S_{wr} - \varepsilon) \quad \text{for } S_l < (S_{wr} + \varepsilon) \quad (4.3)$$

$$p_c = p_e (S_{ek})^{(2-3\lambda)/\lambda} \quad \text{for } S_l \geq (S_{wr} + \varepsilon) \quad (4.4)$$

where

$$S_{ec} = (S_l - S_{wr}) / (1 - S_{wr}) \quad (4.5)$$

$$S_{ek} = (S_l - S_{wr}) / (1 - S_{wr} - S_{gr}) \quad (4.6)$$

and S_l is the liquid saturation, S_{wr} is the residual liquid saturation, S_{gr} is the residual gas saturation, λ is the pore size distribution index, and p_e is the gas entry pressure. To prevent the capillary pressure from increasing to infinity as the effective saturation approaches zero, a linear function is used for $S_l < (S_{lr} + \varepsilon)$, where ε is a small number (Equation 4.3).

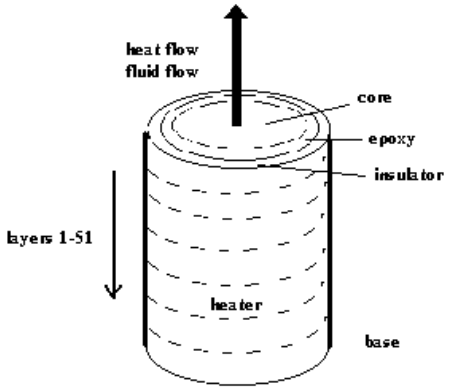

Figure 4.2: Schematic diagram of the 3×51 TOUGH2 model.

4.5 PARAMETER ESTIMATION

Forward Calculation

To avoid time-consuming inverse calculations, forward runs were done first to roughly match the experimental data (temperature, pressure, steam saturation, and heat flux) with simulated results. The sensitivity of the system response to the parameters under investigation (S_{wr}, S_{gr}, λ, and p_e) was determined. However, since these are parameters related to two-phase flow conditions, the system response, as calculated by TOUGH2, showed sensitivity only when there were steam and water present. In the experiment, two-phase conditions were observed after 120 hours from the start of the experiment.

Results of the sensitivity analysis showed that temperature, pressure, and steam saturation were higher at lower S_{wr}. Conversely, temperature, pressure, and steam saturation were lower at higher S_{wr}. At the same water saturation value, the capillary pressure decreased as S_{wr} was increased. Moreover, the temperature, pressure, and steam saturation were higher at lower S_{gr} while they were lower at higher S_{gr}. The capillary pressure did not change with S_{gr} since it is not a function of S_{gr}. At lower values of λ, the temperature, pressure, and steam saturation were lower than at higher values of λ. The relative permeability of water became more concave upwards at lower λ, then became linear at a certain value, after which it became more convex downwards. The capillary pressure increased as λ was decreased. Furthermore, the temperature, pressure, and steam saturation were higher at smaller values of p_e due to the lower capillary pressure required to displace the water by steam.

By trial-and-error a rough fit to the experimental data was obtained at the following values: S_{wr}=0.2, S_{gr}=0.2, λ=0.5, p_e=500 Pa, and ε=0.05. In all the plots given in this paper, T1, P1, Sst1, and HF1 are temperature, pressure, saturation, and heat flux measured at 1 cm from the heater, respectively. T2, P2, Sst2, and HF2 are measured at 2 cm from the heater. T3, P3, Sst3, and HF3 are measured at 3 cm from the heater. Finally, T4, P4, Sst4, and HF4 are measured at 4 cm from the heater.

The measured and simulated temperature data consistently differ by 6-12 ^{o}C from T1 to T4 (Figs. 4.3a and 4.3b). The simulated pressures mimic the observed data from P1 to P4 (Figs. 4.4a and 4.4b), although the differences are still large considering that the gauge pressure measurement range is only ~28,000 Pa. The maximum difference between the measured and calculated pressure values is ~6000 Pa (Fig. 4.4b). In terms of steam saturation, the fit is slightly poor since there are only three sets of steam saturation data to compare the simulated results (Figs. 4.5a and 4.5b). To generate data at the specified observation times, TOUGH2 interpolated between the two measured data points. The real data and the interpolated data points were used to calibrate the model, which involved comparing simulated results with experimental data and minimizing the weighted difference between them. However, the interpolated steam saturation data are not shown on Figures 4.5a and 4.5b. The observed and simulated heat flux data have a good fit at all measurement points except at HF1, where the maximum difference between the observed and calculated data is ~225 W/m^2 (Figs. 4.6a and 4.6b). Relative permeability (Brooks-Corey)

and capillary pressure (Brooks-Corey) curves used to obtain these results are given in Figures 4.7 and 4.8, respectively.

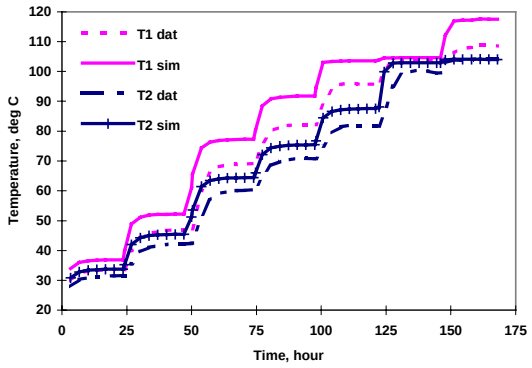

Figure 4.3a: Observed and simulated temperature data at T1 and T2 generated from initial guesses.

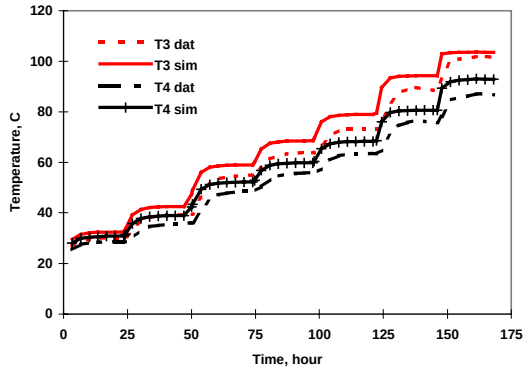

Figure 4.3b: Observed and simulated temperature data at T3 and T4 generated from initial guesses.

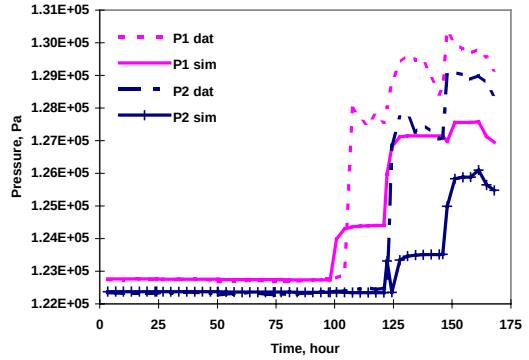

Figure 4.4a: Observed and simulated pressure data at P1 and P2 generated from initial guesses.

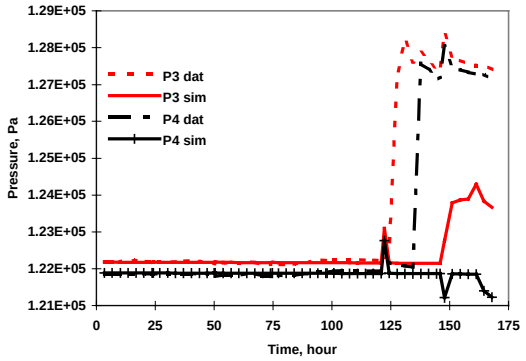

Figure 4.4b: Observed and simulated pressure data at P3 and P4 generated from initial guesses.

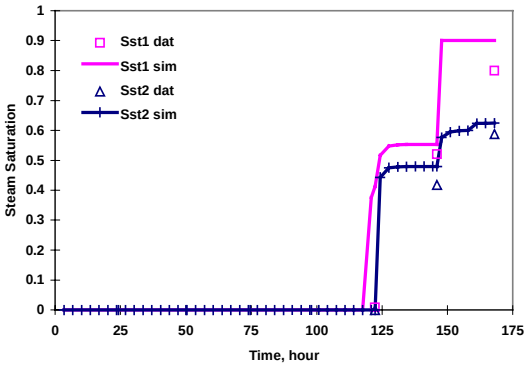

Figure 4.5a: Observed and simulated steam saturation at Sst1 and Sst2 generated from initial guesses.

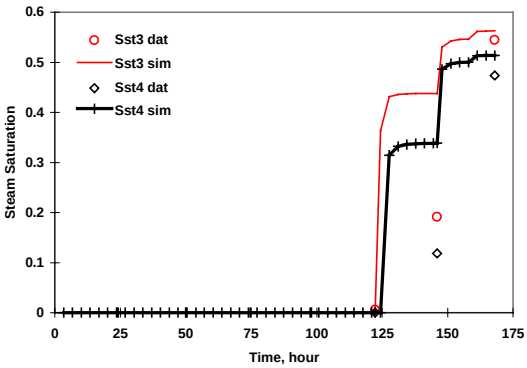

Figure 4.5b: Observed and simulated steam saturation at Sst3 and Sst4 generated from initial guesses.

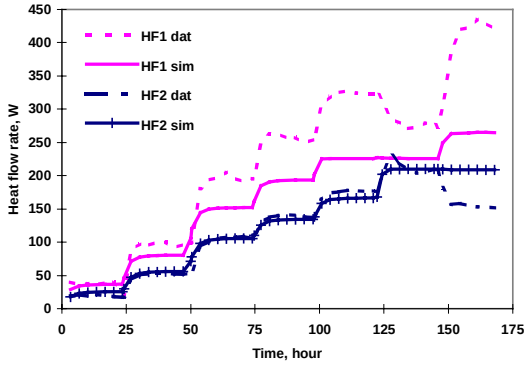

Figure 4.6a: Observed and simulated heat flux data at HF1 and HF2 generated from initial guesses.

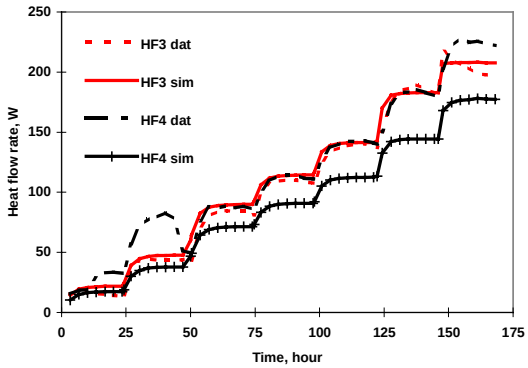

Figure 4.6b: Observed and simulated heat flux data at HF3 and HF4 generated from initial guesses.

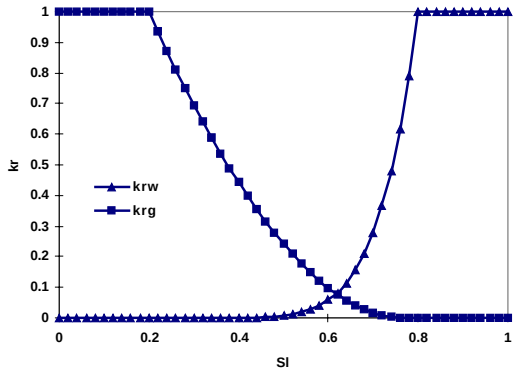

Figure 4.7: Brooks-Corey relative permeability curves at S_{wr}=0.2, S_{gr}=0.2, and λ=0.50, p_e=500 Pa.

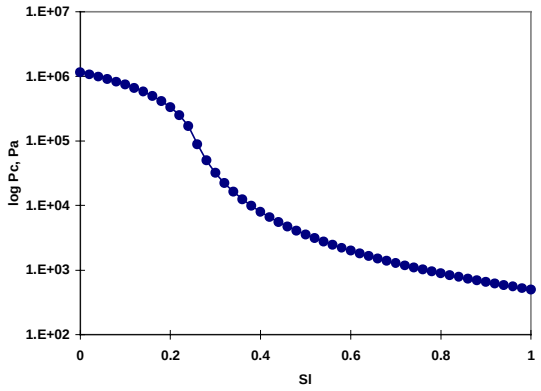

Figure 4.8: Modified Brooks-Corey capillary pressure curve at S_{wr}=0.2, S_{gr}=0.2, λ=0.5, p_e=500 Pa and ε=0.05.

Inverse Calculation

Higher accuracy of the model prediction can be achieved by a combined inversion of all available data since data types contribute to parameter estimation in different degrees during the calibration phase, when simulated data are compared with real data and the weighted difference between them is minimized (Finsterle et al, 1997). The model was calibrated against temperature, pressure, steam saturation, and heat flux (Table 4.2) to estimate S_{wr}, S_{gr}, λ, p_e, thermal conductivity of sandstone, σ_s, thermal conductivity of insulator, σ_i, thermal conductivity of heater insulator (or the base), σ_b, and absolute permeability of sandstone, k. The standard deviation values given in Table 4.2 reflect the uncertainty associated with the measurement errors. Table 4.3 shows a summary of the estimated parameter set.

The parameter estimates remarkably improve the temperature match, and to some extent the pressure match (Figs. 4.9a, 4.9b, 4.10a, and 4.10b). Based on the few measured steam saturation data points available, the fit is also improved by using estimates obtained from inverse calculation (Figs. 4.11a and 4.11b). On the other hand, there is no considerable improvement in the heat flux match (Figs. 4.12a and 4.12b). The Brooks-Corey relative permeability and pressure capillary curves corresponding to the estimated values of S_{wr}, S_{gr}, λ, and p_e are shown in Figures 4.13 and 4.14, respectively. Figure 4.13 suggests that the core is strongly water-wet as indicated by the position of the intersection of the relative permeability curves.

The covariance and correlation matrices are given in Table 4.4, where the diagonal elements give the square of the standard deviation of the parameter estimate, σ_p. σ_p takes into account the uncertainty of the parameter itself and the influence from correlated parameters. In Table 4.5, the conditional standard deviation, σ_p* reflects the uncertainty of one parameter if all the other parameters are known. Hence, σ_p*/σ_p (column 3) is a measure of how independently a parameter can be estimated. A value close to one denotes an independent estimate, while a small value denotes strong correlation to other uncertain parameters. The total parameter sensitivity (column 4) is the sum of the absolute values of the sensitivity

coefficients, weighted by the inverse of individual measurement errors and scaled by a parameter variation (Finsterle et al, 1997).

As shown in Table 4.5, σ_i and σ_b are the most sensitive parameters. Except for σ_b, all parameters cannot be determined independently because they are strongly correlated to one or more of the other parameters (Table 4.3). Moreover, the relatively large standard deviation of the estimated values of λ and p_e are due to the fact that they are closely related as indicated by their comparatively high correlation coefficient (Table 4.3). Also, λ is correlated to p_e since the capillary pressure is dependent on both λ and p_e (Equations 4.3 and 4.4).

Table 4.6 gives the statistical parameters related to the residuals. Comparing the total sensitivity (column 2) of the different observation types, accurate measurements of temperature, pressure, and steam saturation are sufficient to solve the inverse problem, i.e. heat flux data are much less sensitive. The standard deviation values of the final residual (column 3) are of the same order of magnitude as the measurement errors (Table 4. 2) indicating that there are no significant systematic errors present. Lastly, the contribution of each observation type to the final value of the objective function (COF) is relatively evenly distributed suggesting that the choice of weighting factor is reasonable.

4.6 CONCLUSION

It has been demonstrated that it is possible to infer relative permeability using transient experimental data by inverse calculation. Other relative permeability and capillary pressure functions (e.g. van Genuchten) will be used to potentially improve the fit.

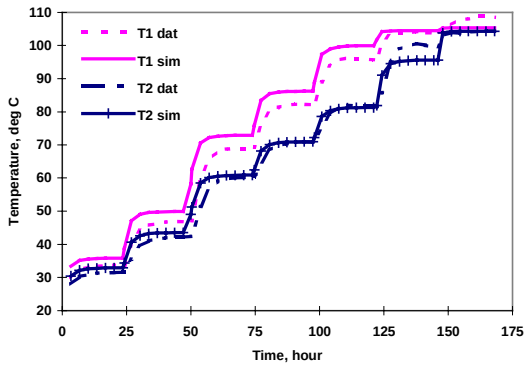

Figure 4.9a: Observed and simulated temperature data at T1 and T2 generated from estimated values.

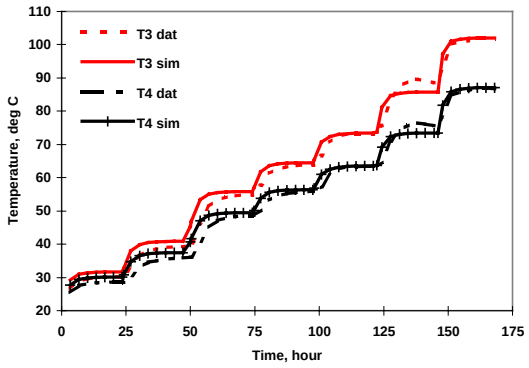

Figure 4.9b: Observed and simulated temperature data at T3 and T4 generated from estimated values.

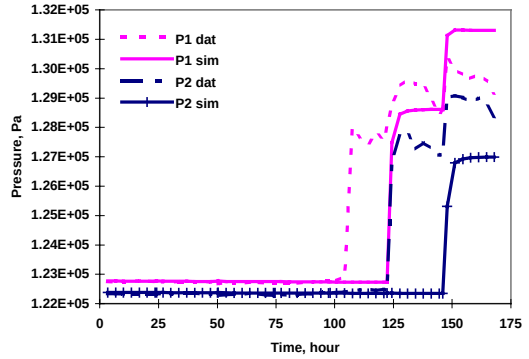

Figure 4.10a: Observed and simulated pressure data at P1 and P2 generated from estimated values.

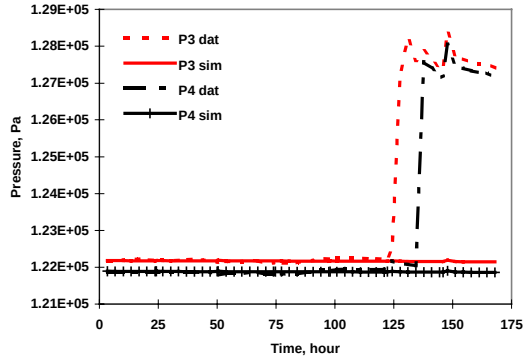

Figure 4.10b: Observed and simulated pressure data at P3 and P4 generated from estimated values.

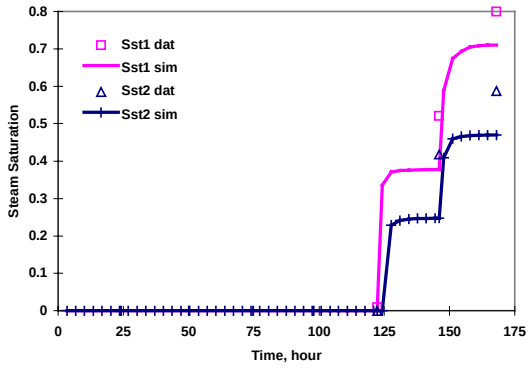

Figure 4.11a: Observed and simulated steam saturation data at Sst1 and Sst2 generated from estimated values.

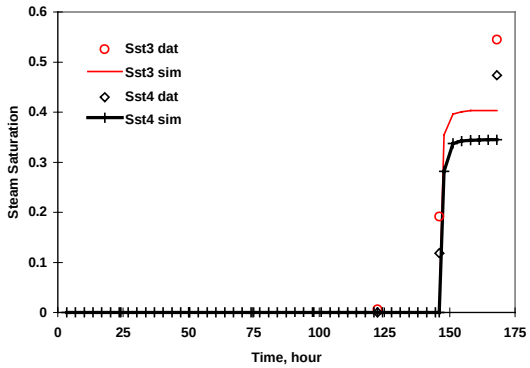

Figure 4.11b: Observed and simulated steam saturation data at Sst3 and Sst4 generated from estimated values.

Table 4.2. Observation used for model calibration.

Data Type	Standard Deviation
Temperature	1 ^{o}C
Pressure	1000 Pa
Steam Saturation	0.01
Heat Flux	20 W/m^2

Table 4.3: Parameter initial guesses and estimated values.

Parameter	Initial Guess	Best Estimate	Difference
σ_s, W/m-C	4.326	4.299	-0.027
σ_I, W/m-C	0.090	0.095	0.005
σ_b, W/m-C	0.125	0.172	0.047
Log k, m^2	-12.07	-12.31	-0.24
S_{wr}	0.200	0.209	0.009
S_{gr}	0.200	0.065	-0.135
λ	0.500	0.343	0.157
Log p_e, Pa	2.70	2.98	-0.28

Table 4.4: Variance-covariance matrix (diagonal and lower triangle) and correlation matrix (upper triangle).

	σ_s	σ_i	σ_b	log k
σ_s	6.3E-3	-0.97	0.12	-8.6E-2
σ_i	-2.7E-4	1.2E-5	-0.20	0.19
σ_b	1.5E-6	-1.1E-7	2.5E-8	0.11
log k	-2.7E-4	2.7E-5	7.2E-7	1.6E-3
S_{wr}	5.1E-4	-2.2E-5	4.1E-7	-5.6E-4
S_{gr}	0.37	-0.17	0.28	-5.2E-6
λ	7.1E-4	-2.6E-5	5.2E-7	-1.2E-3
log p_e	3.2E-4	-2.0E-5	-1.0E-6	-2.9E-3

	S_{wr}	S_{gr}	λ	log p_e
σ_s	0.19	0.21	0.15	3.7E-2
σ_i	-0.18	-0.22	-0.12	-5.4E-2
σ_b	7.5E-2	8.0E-2	5.4E-2	-6.0E-2
log k	-0.41	-5.9E-3	-0.50	-0.68
S_{wr}	1.2E-3	0.51	0.74	0.44
S_{gr}	3.8E-4	4.7E-3	-0.11	-0.45
λ	1.5E-3	-1.4E-4	3.7E-3	0.88
log p_e	1.6E-3	-1.0E-3	5.7E-3	1.1E-2

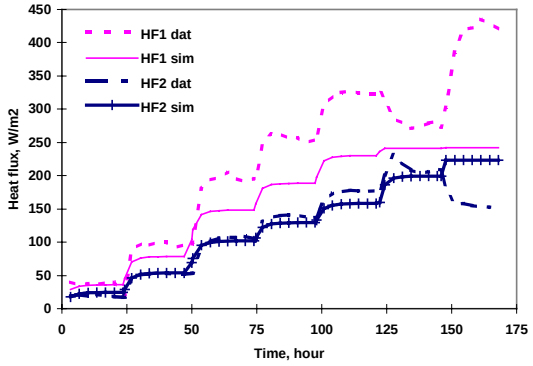

Figure 4.12a: Observed and simulated heat flux data at HF1 and HF2 generated from estimated values.

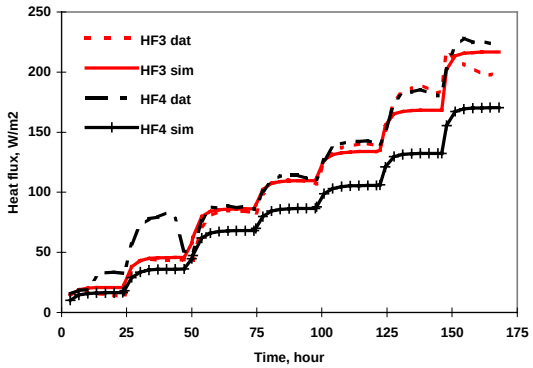

Figure 4.12b: Observed and simulated heat flux data at HF3 and HF4 generated from estimated values

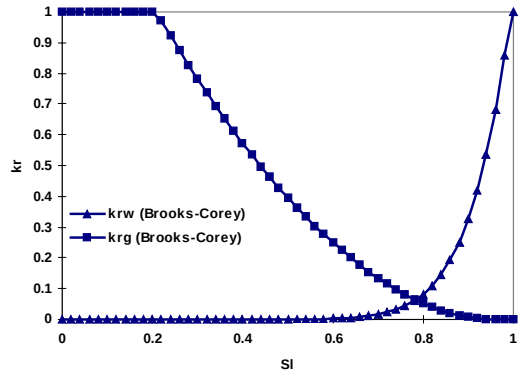

Figure 4.13: Brooks-Corey relative permeability curves at S_{wr}=0.209, S_{gr}=0.065, and λ=0.343.

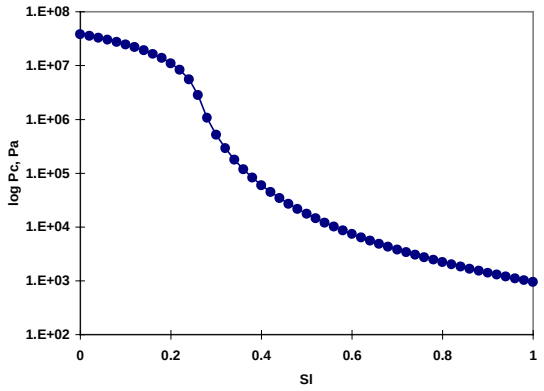

Figure 4.14: Modified Brooks-Corey capillary pressure curve at S_{wr}=0.209, S_{gr}=0.065, λ=0.343, p_e=973 Pa, and ε=0.05.

Table 4.5. Statistical measures and parameter sensitivity.

Parameter	σ_p	σ_p^*/σ_p	Parameter Sensitivity
σ_s	0.079	0.151	1482
σ_i	0.0035	0.151	35302
σ_b	0.00016	0.675	288850
log k	0.04	0.142	2112
S_{wr}	0.0346	0.258	1989
S_{gr}	0.022	0.143	3522
λ	0.061	0.062	4075
log p_e	0.106	0.048	2428

Table 4.6: Total sensitivity of observation, standard deviation of residuals, and contribution to the objective function (COF).

Observation	Sensitivity	Std Dev	COF %
Temperature	1415.8	2.2	22.44
Pressure	1271.3	1460	11.27
Saturation	3164.4	0.01	43.10
Heat flux	265.5	29.3	22.93

5. REFERENCES

Ambusso, W.J.: *Experimental Determination of Steam-Water Relative Permeability Relations*, MS report, Stanford University, Stanford, California (1996).

Amistoso, A.E. and Orizonte, R.G., Jr., 1997, "Reservoir Response to Full Load Operation Palinpinon Production Field Valencia, Negros Oriental, Philippines", Proceedings of 18th PNOC-EDC Geothermal Conference.

Arihara, N.: *A Study of Non-Isothermal Single and Two-Phase Flow Through Consolidated Sandstones*, PhD dissertation, Stanford University, Stanford, California (1976).

Bau, H.M. and Torrance, K. E. (1982). Boiling in low-permeability porous materials. *Int. J. of Heat Mass Transfer* **25**, 45-55.

Bodvarsson, G. (1969). On the temperature of water flowing through fractures. *J. Geophys. Res.* 74(8), 1987-1992.

Bodvarsson, G. (1972). Thermal problems in the siting of reinjection wells. *Geothermics* **2**(1), 63-66.

Bodvarsson, G.S., O'Sullivan, M.J., and Tsang, C.F.: The Sensitivity of Geothermal Reservoir Behavior to Relative Permeability Parameters, *Proceedings*, 6th Workshop on Geothermal Reservoir Engineering, Stanford, CA, Dec. 16-18, 1980.

Bowerman, B.L. and O'Connell, R.T., (1990). Linear Statistical Models: An Applied Approach, 2nd Edition. PWS-KENT Publishing Company, Boston, MA.

Brooks, R.H. and Corey, A.T., (1964). Hydraulic Properties of Porous Media, Colorado State University, Hydro paper No.5.

Chen, J.K., Council, J.R., and Ramey, H.J., Jr.: Experimental Steam-Water Permeability Curves," *GRC Trans.* **2** (1978), pp 102-104.

Clossman, P.J., and Vinegar, J.J.: "Relative Permeability to Steam and Water at Residual Oil in Natural Cores; CT Scan Saturation," SPE paper 17449.

Corey, A.T.: The Interrelations Between Gas and Oil Relative Permeabilities, *Producers Monthly* **19** (1954), pp 38-41.

Council, J.R., and Ramey, H.J., Jr.: Drainage Relative Permeabilities Obtained from Steam-Water Boiling Flow and External Gas Drive Experiments, *GRC Trans.* **3** (1979), pp 141-143.

Drummond, J.E. and McNabb, A. (1972). The heating of cold-water intrusions in a geothermal field. *N. Z. J. Sci.* **15**(4), 665-672.

Eastman, G.Y. (1968): The heat pipe. *Sci. American* **218**, 38-64.

Finsterle, S., 1997. ITOUGH2 Command References Version 3.1, Lawrence Berkeley National Laboratory, Berkeley, Calif.

Finsterle, S., Pruess, K., Bullivant, D.P., and O'Sullivan, M.J. (1997). Application of Inverse Modeling to Geothermal Reservoir Simulation, *Proceedings*, 22rd Workshop on Geothermal Reservoir Engineering, Stanford, Calif.

Fourar, M., Bories, S., Lenormand, R., and Persoff, P.: Two-Phase Flow in Smooth and Rough Fractures: Measurement and Correlation by Porous-Medium and Pipe Flow Models, *Water Resources Research* **29** (11), (1993), pp 3699-3708.

Grant, M.A.: Permeability Reduction Factors at Wairakei, *Proceedings*, AIChE-ASME Heat Transfer Conference, Salt Lake City, Utah (August 1977), pp 15-17.

Grant, M. A. and Studt, F. E. (1981). A conceptual model of the Tongonan geothermal reservoir. *Pap. GEOSEA Conf. 4th, 1981.*

Grindley, G.W. (1965). Wairakei. *New Zealand Volcanology*. 157.

Harper, R.T. and Jordan, O.T., 1985, "Geochemical Changes in Response to Production and Reinjection for Palinpinon-I Geothermal Field, Negros Oriental, Philippines", Proceedings of 7th New Zealand Geothermal Workshop.

Honarpour, M., Koederitz, L.F., and Harvey, A.H.: Empirical Equations for Estimating Two-Phase Relative Permeability in Consolidated Rock, *JPT* (Dec. 1982), pp 2905-2909.

Hornbrook, J.W. and Faulder, D.D. (1993). Parametric analysis of factors affecting injection and production in geothermal reservoirs. *Proc. Stanford Geoth. Workshop* **18**, 53-60.

Horne, R.N., and Ramey, H.J., Jr.: Steam/Water Relative Permeability from Production Data, *GRC Trans.* **2** (1978).

Jansen, F.E. and Kelkar, M.G., 1997, "Application of Wavelets to Production Data in Describing Inter-Well Relationships", paper SPE 38876, presented at 1997 SPE Annual Technical Conference and Exhibition.

Li, K., and Horne, R.N.: Accurate Measurement of Steam Flow Properties, *GRC Trans.* **23** (1999).

Macario, M.E., 1991, "Optimizing Reinjection Strategy in Palinpinon, Philippines Based on Chloride Data", M.S. Thesis, Stanford University, Stanford, CA.

Mahiya, G.F.: *Experimental Measurement of Steam-Water Relative Permeability*, MS report, Stanford University, Stanford, CA (1999).

Monsalve, A., Schechter, R.S., and Wade, W.H.: *Relative Permeabilities of Surfactant/Steam/Water Systems*, Paper SPE/DOE 12661, presented at the Society of Petroleum Engineers Symposium on Enhanced Oil Recovery, Tulsa, Oklahoma, April 1984.

Nathenson, M. (1975). Physical factors determining the fraction of stored energy recoverable from hydrothermal convection systems and conduction dominated areas. *Geol. Surv. Open-File Rep.* (U.S.) 75-525.

Ogden, R.T., 1997, Essential Wavelets for Statistical Applications and Data Analysis. Birkhauser Boston, Cambridge, MA.

Pamatian, P.I., 1997, "Changes in the Apparent Piezometric Levels in the Palinpinon Field as a Response to Twelve Years of Exploitation", Proceedings of 18th PNOC-EDC Geothermal Conference.

Pan, X., Wong, R.C., and Maini, B.B.: *Steady State Two-Phase Flow in a Smooth Parallel Fracture*, presented at the 47th Annual Technical Meeting of The Petroleum Society in Calgary, Alberta, Canada, June 10-12, 1996.

Persoff, P., and Pruess, K.: Two-Phase Flow Visualization and Relative Permeability Measurement in Natural Rough-Walled Fractures, *Water Resources Research* **31** (5), (1995), pp 1175-1186.

Persoff, P., Pruess, K., and Myer, L.: Two-Phase Flow Visualization and Relative Permeability Measurement in Transparent Replicas of Rough-Walled Fractures, *Proceedings,* 16th Workshop on Geothermal Reservoir Engineering, Stanford University, Stanford, CA, Jan. 23-25, 1991, pp 203-210.

Piquemal, J.: Saturated Steam Relative Permeabilities of Unconsolidated Porous Media, *Transport in Porous Media* **17** (1994), pp 105-120.

Pruess, K. (1985). A quantitative model of vapor dominated geothermal reservoirs as heat pipes in fractured porous rock. *Geothermal Resources Council: Transactions* 9(II), 353-361.

Pruess, K., (1987). TOUGH User's Guide, Lawrence Berkeley National Laboratory, Berkeley, Calif.

Pruess, K., (1991). TOUGH2-A General Purpose Numerical Simulator for Multiphase Fluid and Heat Flow, Report LBL-29400, Lawrence Berkeley National Laboratory, Berkeley, Calif.

Pruess, K. (1991). Grid orientation and capillary pressure effects on the simulation of water injection into depleted vapor zones. *Geothermics* **20**(No.5/6), 257-277.

Pruess, K. and O'Sullivan M. (1992). The effects of capillarity and vapor adsorption in the depletion of vapor-dominated reservoirs. *Proc. Stanford Geoth. Workshop* **17**.

Pruess, K., and Tsang, Y.W.: On Two-Phase Relative Permeability and Capillary Pressure of Rough-Walled Rock Fractures, *Water Resources Research* **26** (9), (1990), pp 1915-1926.

Rangel-German, E., Akin, S., and Castanier, L.M.: Multiphase Flow Properties of Fractured Porous Media, paper SPE 54591, presented at the SPE Western Regional Meeting, Anchorage, AK, May 26-28, 1999.

Romm, E.S.: *Fluid Flow in Fractured Rocks*, Nedra Publishing House, Moscow, (English translation, Blake, W.R., Bartlesville, OK, 1972).

Rossen, W.R., and Kumar, A.T.A.: Single- and Two-Phase Flow in Natural Fractures, paper SPE 24915, presented at the 67th Annual Technical Conference and Exhibition of the Society of Petroleum Engineers, Washington, DC, Oct. 4-7, 1992.

Sanchez, J.M., and Schechter, R.S.: Comparison of Two-Phase Flow of Steam/Water through an Unconsolidated Permeable Medium, *SPE Reservoir Engineering*, Aug. (1990), pp 293-300.

Satik, C. (1997), A Study of Boiling in Porous Media, Proc. 19th New Zealand Geothermal Workshop, Auckland, NZ.

Satik, C.: A Measurement of Steam-Water Relative Permeability, *Proceedings*, 23rd Workshop on Geothermal Reservoir Engineering, Stanford University, Stanford, CA (1998).

Satik, C., Walters, M. and Horne, R. N. (1996). Adsorption characteristics of rocks from the vapor-dominated reservoir at the Geysers, CA. *Proc. Stanford Geoth. Workshop* **21**, 469-479.

Sondergeld, C. H. and Turcotte, D. L. (1977). An experimental study of two-phase convection in porous medium with applications to geological problems. *J. Geophys. Res.* **82**(14), 2045-2053.

Sorey, M.L., Grant M.A. and Bradford E., (1980). Nonlinear Effects in Two Phase Flow to Wells in Geothermal Reservoirs. *Water Resources Research*, Vol. 16 No. 4, pp 767-777.

Tabachnick, B.G. and Fidell, L.S., 1996, *Using Multivariate Statistics*. HarperCollins College Publishers, New York.

Tovar, R.A.: *Measurement of Relative Permeability for Steam-Water Flow in Porous Media*, MS report, Stanford University, Stanford, CA (1997).

Verma, A., and Pruess, K.: Enhancement of Steam Phase Relative Permeability Due to Phase Transformation Effects in Porous Media, *Proceedings*, 11th Workshop on Geothermal Reservoir Engineering, Stanford University, Stanford, CA (1986).

Wang, C.T., and Horne, R.N.: Boiling Flow in a Horizontal Fracture, submitted to *Geothermics*, 1999.

White, D. E. L., Muffler, J. P. and Truesdell, A. H. (1971). Vapor-dominated hydrothermal systems compared with hot-water systems. *Econ. Geol.* **66**,75-97.